Journal of Zhejiang University-SCIENCE A (Applied Physics & Engineering) in press
www.jzus.zju.edu.cn; www.springer.com/journal/11582
E-mail: jzus_a@zju.edu.cn

Research Article

https://doi.org/10.1631/jzus.A2300338

Numerical study on local failures of reinforced concrete slabs against underwater close-in explosions

Fei ZHOU[1], Hedong LI[2], Hao WU[1]✉

[1]*College of Civil Engineering, Tongji University, Shanghai, 200092, China*
[2]*School of Civil Engineering and Architecture, Zhejiang Sci-Tech University, Hangzhou, 310018, China*

Abstract: Reinforced concrete (RC) slabs are the primary load-carrying member of underwater facilities. They can suffer severe local failures such as cratering, spalling, or breaching as a result of underwater close-in (UWCI) explosions. In this study, we established a fully validated high-fidelity finite element analysis approach to precisely reproduce the local failures of RC slabs after a UWCI explosion. A recently proposed dynamic constitutive model is briefly introduced to describe wet concrete. The effects of free water content on the material properties, including the tensile/compressive strength, elastic modulus, strain rate effect, failure strength surface, and equation of state, are comprehensively calibrated based on existing test data. The calibrated material parameters are then verified by a single-element test. A high-fidelity finite element analysis (FEA) approach of an RC slab subjected to a UWCI explosion is established using an arbitrary Lagrangian-Eulerian (ALE) algorithm. Simulating previous UWCI explosion tests on RC orifice targets and underwater contact explosion tests on saturated concrete slabs showed that the established FEA approach could accurately reproduce the pressure-time history in water and damage patterns, including the cracking, cratering, and spalling, of the RC orifice target and saturated concrete slab. Furthermore, parametric studies conducted by simulating an RC slab subjected to a UWCI explosion showed that: (i) the local failure of an RC slab enlarges with increased charge weight, reduced standoff distance, and reduced structural thickness; (ii) compared to a water-backed RC slab, an air-backed RC slab exhibits much more obvious local and structural failure. Lastly, to aid the anti-explosion design of relevant underwater facilities, based on over ninety simulation cases empirical formulae are summarized to predict local failure modes, i.e., no spall, spall, and breach, of water- and air-backed RC slabs subjected to a UWCI explosion.

Key words: Reinforced concrete slab; Underwater close-in explosion; Saturated concrete; Failure modes; Constitutive model; Numerical simulation

1 Introduction

Underwater infrastructure, such as tunnels crossing rivers or oceans, submarine pipelines, and caisson wharves, perform essential economic and social roles in guaranteeing the transportation of people, goods, water, natural gas, electric power, etc. In recent decades, terrorist attacks using explosives have posed an increasingly severe threat worldwide (Magnus et al., 2018). As a result, the safety of these critical underwater structures is a cause of great public concern. For example, in September 2022 several leaks were discovered in the Nord Stream 1 and 2 submarine gas pipelines (Nord Stream Press Releases, 2022). They were caused by intentional sabotage by underwater explosion, and attracted broad international interest. Reinforced concrete (RC) slabs are the primary load-carrying member in underwater facilities. Thus, examining the resistance of RC slabs to underwater explosions is essential. In particular, a close-in explosion scenario is more dangerous than a far-field explosion and more complex to analyze since it involves a strain rate and pressure-dependent material constitutive model, instantaneous interaction between detonation products and the RC structure, propagation of an intense shock wave, and various local failure modes in the incident and distal free surfaces (Costanzo 2011; Sanders et al. 2021). Predicting the local failure modes of an RC slab subjected to an underwater close-in (UWCI) explosion is fundamental to the anti-explosion design of underwater infrastructure,

✉ Hao WU, wuhaocivil@tongji.edu.cn
Fei ZHOU, https://orcid.org/0000-0001-6368-0259

Received June 30, 2023; Revision accepted Aug. 27, 2023; Crosschecked

but is yet to be achieved.

Over recent decades, a lot of in-air close-in explosion tests have been conducted on RC structures to study the influence of the charge weight W (McVay, 1988; Shi et al., 2015; 2020), standoff distance R (McVay, 1988; Kumar et al., 2020), structural thickness T (McVay, 1988), concrete compressive strength f_c (McVay, 1988), reinforcement setting (McVay, 1988), and scale size (Wang et al., 2012). The local failure modes of an RC slab include cratering on the incident surface, spall in the distal surface, and breach throughout the cross-section, and are strongly affected by W, R, and T. To predict the failure modes of the RC slab, McVay (1988) conducted lots of in-air close-in explosion tests and proposed an empirical formula that depends on the scaled distance $R/W^{1/3}$ and scaled thickness $T/W^{1/3}$. Besides, the UFC 3-340-02 code (UFC, 2008) compiled and analyzed the existing test data and summarized the threshold cures to distinguish the failure modes in the distal free surfaces, i.e., no spall, spall (no breach), and breach. However, these predictive formulae (McVay, 1988; UFC, 2008) are not applicable to an underwater explosion. Compared to an in-air explosion, an underwater explosion would cause much more severe damage to the concrete structure because the water and air have different density and sound speed, and the explosive detonation induces both a shock wave and a bubble pulse in water (Cole, 1948; Rajendran and Lee, 2009; Hu et al., 2017).

Recently, the dynamic response of an RC slab subjected to a UWCI explosion has attracted increasing research interest. Zhao et al. (2021) conducted in-air and underwater contact explosion tests on 50–100 mm-thickness RC slabs using 6–50 g rock emulsion explosives. They found that an underwater contact explosion causes more severe damage to RC slabs than an in-air contact explosion, and the damage patterns of RC slabs were affected by the boundary condition, charge shape, and steel reinforcement. Yang et al. (2019; 2022; 2023a) experimentally observed the damage patterns of 60 mm-thickness RC slabs of variable concrete compressive strength, i.e., 33 and 38 MPa, and structural span, i.e., 500 and 1000 mm, subjected to an underwater contact explosion of 6 g TNT, and established high-fidelity numerical models according to the corresponding experimental observations. Yang et al. (2023b) experimentally assessed the performance of two RC orifice targets subjected to detonation of 8-g emulsion explosives at their entrance. Both the damage pattern or the RC orifice and the pressure-time history of the water were obtained and adopted to validate the numerical approach based on an arbitrary Lagrangian-Eulerian (ALE) algorithm. Using 2.5–10 g TNT explosives, Wen et al. (2023) conducted underwater contact explosion tests on saturated concrete slabs with dimensions of ϕ400 mm×80 mm. They found that the crater in the front surface was smaller than the spall in the rear surface, and the local failure increased with an increasing mass of TNT. They proposed an improved concrete model to account for the mechanical properties of the saturated concrete and numerically reproduced the damage modes of the saturated concrete slabs. The above tests helped elucidate the failure mechanism of concrete structures subjected to underwater explosions. Nevertheless, there were still insufficient test data to derive a predictive formula to distinguish the local failure modes of an RC slab under a UWCI explosion.

Experimental study is time-consuming, expensive, and may have serious security issues. Based on commercial hydrocodes, such as LS-DYNA (Hallquist, 2006) and AUTODYN (Southpointe, 2020), the high-fidelity finite element analysis (FEA) approach can be used to overcome these obstacles. Once validated by benchmark tests in terms of the underwater load and concrete material model, it can precisely reproduce the dynamic response of an RC structure subjected to a UWCI explosion (Yang et al., 2019; 2022; 2023a; 2023b; Wen et al., 2023). This approach can be used in simulations to examine the influence of critical parameters, such as W, R, and T. Zhao et al. (2018) adopted the coupled finite element and smoothed particle hydrodynamics (FEM-SPH) method and numerically studied the damage patterns of RC slabs subject to in-air and underwater contact explosions. Results showed that the crater and spall dimensions of RC slabs and the plastic strain of steel reinforcement subject to an underwater contact explosion are larger than those of an in-air contact explosion. Yang et al. (2022; 2023a) used the ALE algorithm and evaluated the resistance of air-backed RC slabs and carbon fiber-reinforced polymer (CFRP) retrofitted RC slabs against an underwater contact explosion. They found that the resistance of the

air-backed RC slab was inferior to that of the water-backed RC slab and could be significantly enhanced by CFRP retrofitting. Chen et al. (2023) established a high-fidelity FEA approach by validating the underwater load and concrete material model. They numerically studied the dynamic response of an air-backed RC slab subjected to a UWCI explosion. They found that the damage to the RC slab increased with increasing W and decreasing R, and the higher f_c and reinforcement ratio resulted in higher anti-explosion resistance. The structural damage modes defined according to the support rotation angle of the RC were further assessed for the R=2 m and W=0.2 kg UWCI explosion scenario.

In general, in terms of RC structures subjected to underwater explosion, the previous numerical simulations had the following limitations: (i) most studies focused on the structural response of the RC slab, while the local failure modes remain to be studied in detail; (ii) a robust dynamic constitutive model of concrete is needed to describe the local failure modes. The commercial constitutive models commonly used in previous studies have limitations in describing the dynamic tensile property (Tu and Lu, 2009; Kong et al., 2018; Huang et al., 2020a; Xu et al., 2020); (iii) the free water content in concrete has evident effects on its mechanical properties (Chen et al., 2023), such as the failure strength surface, strain rate effect, and equation of state (EOS), which were rarely considered in previous studies.

To address these research gaps, here we present a numerical study of the local failure of RC slabs subjected to a UWCI explosion. First, an improved dynamic constitutive model proposed by the authors (Zhou et al., 2023c) is introduced, which is embedded in the LS-DYNA as a user-defined material model. To precisely capture the mechanical properties of wet concrete at high strain rates and hydrostatic pressures, the model comprehensively calibrates the material parameters for concrete, considering the effect of free water content. Then, the high-fidelity FEA approach of an RC slab subjected to UWCI explosion is established based on the ALE algorithm. Its capacity to reproduce the pressure-time history in water and the damage pattern of concrete is validated by simulating the previous UWCI explosion test on the RC orifice target and the underwater contact explosion test on the saturated concrete slab. Next, the model is used to conduct numerical simulations of the RC slab under a UWCI explosion and examine the parametric influence of charge weight, standoff distance, structural thickness, reinforcement ratio, concrete compressive strength, and water/air-back conditions. Finally, a formula is summarized for predicting the local failure modes of RC slabs subjected to a UWCI explosion based on numerical simulations, which will serve as a useful reference for the anti-explosion design of underwater facilities.

2 Constitutive model of concrete

Considering that concrete models in commercial hydrocodes have inherent limitations in describing dynamic tensile failures (Tu and Lu, 2009; Kong et al., 2018), in this study we used an improved dynamic constitutive model recently proposed by Zhou et al. (2023c) to predict the damage pattern of an RC structure under a UWCI explosion. The proposed model captures the critical mechanical properties of concrete, including the nonlinear failure strength and EOS, Lode-dependence, strain rate effect, shear dilation, and damage caused by shear deformation and volumetric compaction. It has already been extended to describe the damage pattern and structural response of ultra-high performance concrete under projectile penetration, drop hammer impact, and far-field explosion loadings (Zhou et al., 2022; 2023a). In this section we briefly introduce the proposed model and systematically calibrate the material parameters of wet concrete.

2.1 Dynamic failure strength surface

It is essential to use a rational failure strength surface to describe the nonlinear relation between the failure strength and the hydrostatic pressure P (Zhou and Wu 2023). Fig. 1 shows the failure strength surface, which contains tensile ($\sigma_1\geq\sigma_2\geq\sigma_3\geq0$), tensile-to-compressive ($\sigma_1\geq0\geq\sigma_3$), and compressive ($0\geq\sigma_1\geq\sigma_2\geq\sigma_3$) regions. Y represents the failure equivalent stress, and σ_i is the principal stress (i=1, 2, 3).

In the compressive region, the proposed model adopts the 3D hyperbolic failure surface (Zhou et al., 2023c) given in Eq. (1). It has an asymptote line of (P, Y)=(+∞, $S_{\max}(0.25+0.75\eta_h)$) and interacts the σ_1=0 plane and P axis at (P, Y)=($2\cos\theta f_{cc}/3$, f_{cc}) and

($P_0\eta_s\eta_c^v$, 0), respectively, according to which it derives the expressions of a_1 and a_2. The Lode-angle θ, principal stress ratio α, and invariants of stress deviator tensor, i.e., J_2 and J_3, can capture the stress state. The damage functions η_h, η_s, and η_c^v describe the compressive strain hardening, compressive strain softening, and volumetric compaction damage on compressive strength, respectively. In Eq. (1c), f_c^{α} is the biaxial compressive strength suggested by Kupfer and Gerstle (1973), where f_c is the uniaxial compressive strength and f_{bc} is the equal-biaxial compressive strength. Based on f_c^{α}, f_{cc} further considers the damage functions, i.e., η_h, η_s, and η_c^v, and the $\sqrt{1+\alpha^2}-\alpha$ term caused by transforming f_c^{α} from σ_1–σ_3 to $\sqrt{3J_2}$.

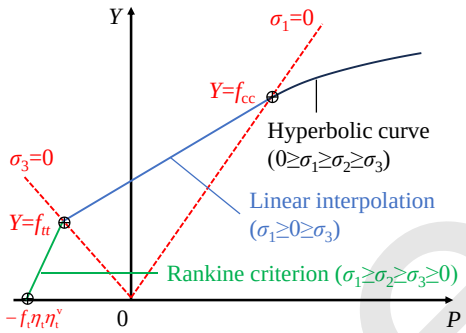

Fig. 1 Sketch diagram of failure strength surface (Zhou et al., 2022; 2023a; 2023b; 2023c)

$$Y=\sqrt{3J_2}=f_{cc}+\frac{P-\frac{2}{3}\cos\theta f_{cc}}{a_1+a_2\left(P-P_0\eta_s\eta_c^v\right)},$$

$$\text{for } P>\frac{2}{3}\cos\theta f_{cc} \quad (1a)$$

$$a_1=\frac{2}{3}\cos\theta-\frac{P_0\eta_s\eta_c^v}{f_{cc}},$$

$$a_2=\frac{1}{S_{max}\left(0.25+0.75\eta_h\right)-f_{cc}} \quad (1b)$$

$$f_{cc}=f_c^{\alpha}\left(0.45+0.55\eta_h\right)\eta_s\eta_c^v\sqrt{1+\alpha^2}-\alpha,$$

$$f_c^{\alpha}=f_c\frac{1+\alpha\left(4f_{bc}/f_c-1\right)}{\left(1+\alpha\right)^2} \quad (1c)$$

$$\theta=\frac{1}{3}\text{acos}\left(\frac{3\sqrt{3}}{2}\frac{J_3}{J_2^{1.5}}\right),$$

$$\alpha=\frac{\sigma_1-\sigma_2}{\sigma_1-\sigma_3}=\frac{\cos\left(2\pi/3-\theta\right)-\cos\left(2\pi/3+\theta\right)}{\cos\theta-\cos\left(2\pi/3+\theta\right)} \quad (1d)$$

In the tensile region, the proposed model uses the Rankine criterion (Rankine, 1876), i.e., Eq. (2), which interacts with the σ_3=0 plane and P axis at (P, Y)=($2\cos(2\pi/3+\theta)f_{tt}/3$, f_{tt}) and ($-f_t\eta_t\eta_t^v$,0), respectively. The damage functions η_t and η_t^v describe the tensile strain softening and volumetric compaction damage, respectively, on the tensile strength. f_{tt} is the $\sqrt{3J_2}$ of the uniaxial tensile strength f_t with damage functions, i.e., $f_{tt}=f_t\eta_t\eta_t^v\sqrt{1+\alpha^2}-\alpha$.

$$Y=\sqrt{3J_2}=\frac{3\left(P+f_t\eta_t\eta_t^v\right)}{2\cos\theta},$$

$$\text{for } -f_t\eta_t\eta_t^v\le P\le\frac{2}{3}\cos\left(\frac{2}{3}\pi+\theta\right)f_{tt} \quad (2)$$

In the tensile-to-compressive region, the failure strength surface Eq. (3) is obtained by interpolating linearly between the boundaries of the tensile and compressive regions.

$$Y=\sqrt{3J_2}=f_{tt}+\frac{P-\frac{2}{3}\cos\left(\frac{2}{3}\pi+\theta\right)f_{tt}}{\frac{2}{3}\cos\theta f_{cc}-\frac{2}{3}\cos\left(\frac{2}{3}\pi+\theta\right)f_{tt}}\left(f_{cc}-f_{tt}\right)$$

$$\text{for } \frac{2}{3}\cos\left(\frac{2}{3}\pi+\theta\right)f_{tt}<P\le\frac{2}{3}\cos\theta f_{cc} \quad (3)$$

Under dynamic loadings, the proposed model uses the radial enhancement approach (Malvar et al., 1997) presented in Eq. (4) to describe the strain rate effect. The parameters Y_{DIF} and P_{DIF} denote the Y and P containing the strain rate effect, i.e., the dynamic increase factor (DIF).

$$Y_{DIF}(P_{DIF})=\text{DIF}\cdot Y(P),\text{ where } P=P_{DIF}/\text{DIF} \quad (4)$$

2.2 Damage functions

The proposed model considers the damage from shear deformation, i.e., η_h, η_s, and η_t, and volumetric compaction, i.e., η_c^v and η_t^v, and defines the com-

pressive, tensile, volumetric compressive, volumetric tensile, and total damage as D_c=1–η_s, D_t=1–η_t, D_{vc}=1–η_c^v, D_{vt}=1–η_t^v, and D=1–(1–D_c)(1–D_t)(1–D_{vc})(1–D_{vt}), respectively. Eq. (5) gives the damage functions to describe the compressive strain hardening η_h, compressive strain softening η_s (Sargin, 1971), and tensile strain softening η_t (Hordijk, 1991). Parameter A affects the compressive strain softening slop, η_s accumulates once η_h reaches 1, and ε_{frac}=0.007 is the fracture strain (Xu and Wen, 2016).

$$\eta_h = 1-\left[1-\min\left(\lambda_h,1\right)^{0.8}\right]^{1.8}, \text{ and}$$

$$\eta_s = \max\left[\frac{1+\lambda_s+(A-1)(1+\lambda_s)^2}{A(1+\lambda_s)^2-\lambda_s}, \frac{f_t}{f_c}\right] \quad (5a)$$

$$\eta_t = \left[1+27\left(\frac{\lambda_t}{\varepsilon_{frac}}\right)^3\right]\exp\left(-6.93\frac{\lambda_t}{\varepsilon_{frac}}\right) - 28\frac{\lambda_t}{\varepsilon_{frac}}\exp(-6.93) \quad (5b)$$

Eq. (6) presents the equivalent plastic strain λ, i.e., λ_h, λ_s, and λ_t, to accumulate these shear deformation damage functions, where $\Delta\varepsilon_e^p$ is the effective plastic strain $\sqrt{2\Delta\varepsilon_{ij}^p\Delta\varepsilon_{ij}^p/3}$, $\Delta\varepsilon_1^p$ denotes the maximum principal plastic strain, and d_1^s, d_1^h, and d_2 are damage parameters. It uses a stress state-related parameter β to consider the continued transition from compression to tension. As shown in Eq. (7), m is the value of β when P=0, and β_c and β_t are stress state-related interpolation coefficients.

$$\lambda_h = \sum\frac{\beta\Delta\varepsilon_e^p}{\mathrm{DIF}\cdot d_1^h\left[1+\max\left(P,0\right)/f_t\right]^{d_2}},$$

$$\lambda_s = \sum\frac{\beta\Delta\varepsilon_e^p}{\mathrm{DIF}\cdot d_1^s\left[1+\max\left(P,0\right)/f_t\right]^{d_2}},$$

$$\lambda_t = \sum(1-\beta)\Delta\varepsilon_1^p \quad (6)$$

$$\beta = m-m\beta_t+(1-m)\beta_c, \text{ where}$$

$$\beta_t = \max\left\{0,\min\left(1,\frac{1.5P/\sqrt{3J_2}}{\cos(\theta+2\pi/3)}\right)\right\},$$

$$\beta_c = \max\left\{0,\min\left(1,\frac{1.5P/\sqrt{3J_2}}{\cos\theta}\right)\right\} \quad (7)$$

Eq. (8) presents the volumetric damage functions summarized from experimental observations (Cui et al., 2017), where f_d reflects the contribution of stress state, P_{DIF}^{max} is the maximum pressure during calculation, and the superscripts 'old' and 'new' denote parameters in the current and previous time steps, respectively.

$$\eta_c^v = 1-\sum f_d\left(r_c^{old}-r_c^{new}\right),$$

$$\eta_t^v = 1-\sum f_d\left(r_t^{old}-r_t^{new}\right) \quad (8a)$$

$$r_c = \max\left(1,\frac{P_{DIF}^{max}}{f_c}\right)^{\frac{-0.007f_c}{\mathrm{MPa}}},\ r_t = \max\left(1,\frac{P_{DIF}^{max}}{f_c}\right)^{\frac{-0.3f_t}{\mathrm{MPa}}},$$

$$f_d = \max\left[0,1-\frac{\cos\theta}{1.5P/\sqrt{3J_2}}\right] \quad (8b)$$

2.3 EOS and plastic flow rule

As identical to the Karagozian & Case Concrete model (Malvar et al., 1997), the proposed model uses the tabulated EOS (*EOS_8 in LS-DYNA) to account for the nonlinear relation between volumetric strain μ and hydrostatic pressure P_{DIF}, as presented in Eq. (9) and Fig. 2. The input parameters (μ_n, P_n) define the plastic compaction path and $K_{u,n}$ determines the corresponding elastic unloading/reloading path.

$$\begin{cases} P_{DIF} = \dfrac{\mu-\mu_n}{\mu_{n+1}-\mu_n}\left(P_{n+1}-P_n\right) \\ K_u = \dfrac{\mu-\mu_n}{\mu_{n+1}-\mu_n}\left(K_{u,n+1}-K_{u,n}\right) \end{cases}, \text{ for } \mu_n<\mu\le\mu_{n+1} \quad (9)$$

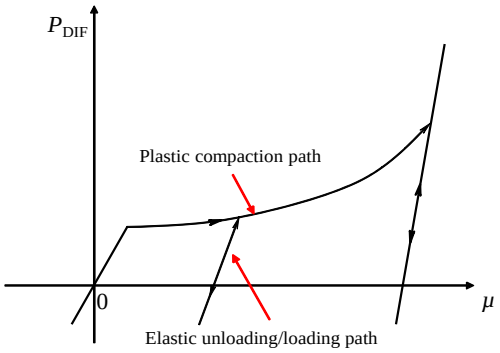

Fig. 2 Sketch diagram of the equation of state (EOS) (Zhou et al., 2022; 2023a; 2023b; 2023c)

The proposed model uses the radial return approach (Simo and Hughes, 1998) to update the stress tensor. It uses an independent plastic potential function to describe the shear dilation of concrete, which is the 3D hyperbolic failure surface at the initial state (η_h=0 and $\eta_s=\eta_c^y$=1) (Zhou et al., 2023c). The proposed model is implemented in LS-DYNA (Version R5.1.1) as a user-defined material model, based on which the following simulations can be conducted.

2.4 Material parameters

The free water content w affects the mechanical properties of concrete. It is defined as $w=(M^w-M)/(M^s-M)$, where M is the mass of dry concrete, and the superscripts w and s refer to the wet and saturated concrete, respectively. Zhao and Wen (2018) suggested the empirical formulae $f_c^w=(1-0.2w)f_c$ and $f_t^w=(1-0.2w)f_t$ used in this study to capture the uniaxial compressive and tensile strength, respectively, of wet concrete. Wu et al. (2012) found that the free water content increases the elastic modulus E. Fig. 3 presents the test data of concrete with variable water content at a strain rate of 10^{-6} s^{-1}, where the elastic modulus of wet concrete is determined as $E^w=(1+0.35w)E$ through linear fitting. The elastic modulus is $E=4730f_c^{0.5}$ according to Malvar et al. (1997). Biaxial compressive strength is also affected by the free water content (Wang et al., 2016).

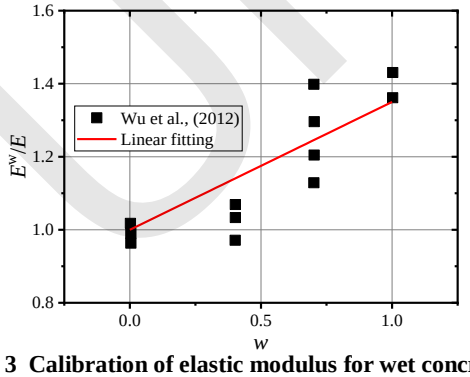

Fig. 3 Calibration of elastic modulus for wet concrete

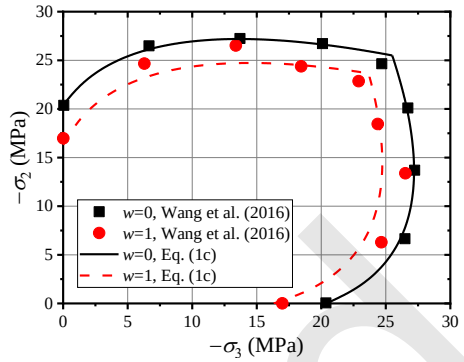

Fig. 4 Comparisons of biaxial compressive strength between Eq. (1c) and test results (Wang et al., 2016)

Fig. 4 shows comparisons of the biaxial compressive strength between predictions from Eq. (1c) and test results of Wang et al. (2016), where the equal-biaxial compressive strength of dry and wet concrete are $f_{bc}=1.25f_c$ and $f_{bc}^w=(1.25+0.2w)f_c^w$, respectively.

Malecot et al. (2019) experimentally observed the influence of the water content on the triaxial failure strength of concrete. Fig. 5 compares the failure strength surface from the test results (Malecot et al., 2019) with the predictions from the proposed model. The calibrated failure strength surface parameters are $P_0=-0.33f_c$ and S_{max}=2600 MPa for dry concrete, and $P_0^w=P_0(1-0.75w)$ and $S_{max}^w=S_{max}(1-w)^{1.44}+9.2f_cw^{1.44}$ for wet concrete. This shows that the calibrated parameters agree well with the test results of concrete with a compressive strength of 28–80 MPa and free water content of $0\le w\le 1$.

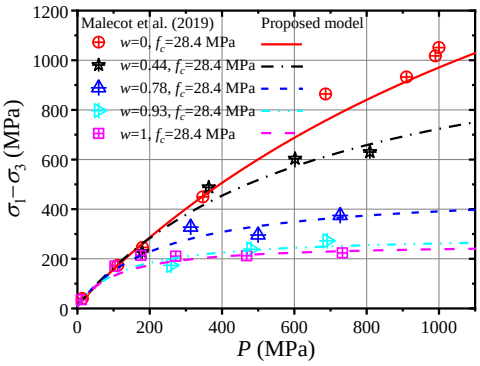

(a)

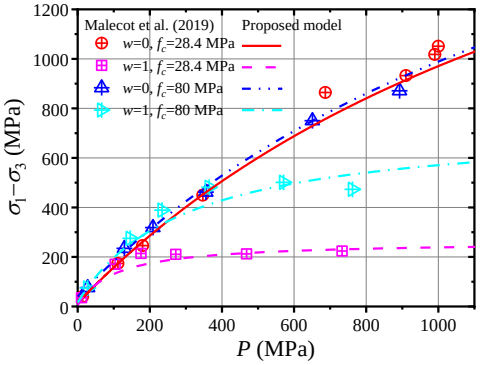

(b)

Fig. 5 Comparisons of triaxial compressive strength between predictions and test results (Malecot et al., 2019)

The dynamic behavior of concrete could be affected by many factors, such as the free water content (Zhao and Wen, 2018) and temperature (Gong et al. 2023). The DIFs under tensile and compressive loadings are defined as the $\mathrm{DIF_t}$ and $\mathrm{DIF_c}$, respectively (Eq. (10)). Xu and Wen (2013) proposed the empirical $\mathrm{DIF_t}$ formulae for dry concrete. To consider the influence of free water content, Zhao and Wen (2018) suggested the $\mathrm{DIF_t}$ of wet concrete, i.e., $\mathrm{DIF_t^w}$. The parameters of dry concrete are S=0.8, F_m=10, W_x=1.6, W_y=5.5, and $\dot{\varepsilon}_0$ =1.0 $\mathrm{s^{-1}}$ (Xu and Wen, 2013), while S and W_x are re-calibrated as S=1.1 and W_x=1.75 based on the dynamic tensile tests of Ross et al. (1996) and Klepaczko and Brara (2001). For wet concrete, Zhao and Wen (2018) obtained C=0.15 through data fitting, which agrees with the test results (Ross et al., 1996; Klepaczko and Brara, 2001), as shown in Fig. 6. In addition, Eq. (10c) gives the DIF for compression of wet concrete, i.e., $\mathrm{DIF_c^w}$ (Zhao and Wen, 2018).

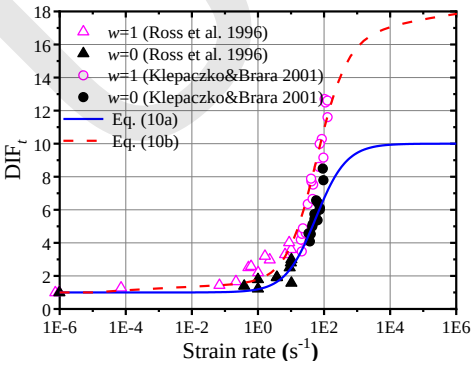

Fig. 6 Comparisons of DIFt between Eq. (10) and test results (Ross et al., 1996; Klepaczko and Brara, 2001)

$$\mathrm{DIF_t}=\left\{\left[\tanh\left(\left(\log\left(\frac{\dot{\varepsilon}}{\dot{\varepsilon}_0}\right)-W_\mathrm{x}\right)S\right)\right]\left(\frac{F_\mathrm{m}}{W_\mathrm{y}}-1\right)+1\right\}W_\mathrm{y} \quad (10a)$$

$\mathrm{DIF_t^w}=g\left(w,\dot{\varepsilon}\right)\mathrm{DIF_t}$, where

$$g\left(w,\dot{\varepsilon}\right)=2-\left(1+Cw\right)^{\max\left(0,-\log\dot{\varepsilon}-5\right)} \quad (10b)$$

$$\mathrm{DIF_c^w}=1+\left(\mathrm{DIF_t^w}-1\right)f_\mathrm{t}^\mathrm{w}/f_\mathrm{c}^\mathrm{w} \quad (10c)$$

The test of Malecot et al. (2019) shows that wet concrete under volumetric compaction is stiffer than dry concrete. Previously, Huang et al. (2020b) and Forquin et al. (2015) calibrated the EOS of dry and wet concrete according to hydrostatic and oedometric compaction tests, respectively. In this study, the parameters of the tabulated EOS for dry and wet concrete were calibrated based on a hydrostatic compaction test (Malecot et al., 2019), in which the elastic modulus of dry and wet concrete was 32 GPa and 42 GPa, respectively (Malecot et al., 2019; Forquin et al., 2015), respectively. Fig. 7 compares the calibrated EOSs and the corresponding test results, and shows that the calibrated EOSs are close to the test results.

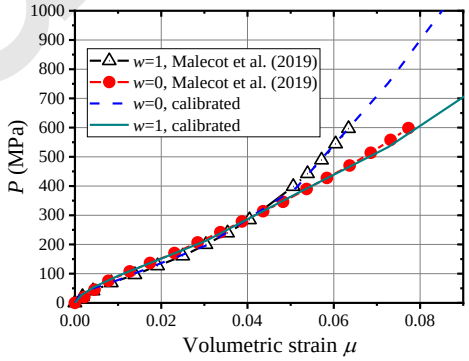

Fig. 7 Comparisons of EOS between the calibrated parameters and test results (Malecot et al., 2019)

Tables 1 and 2 list the calibrated parameters of the proposed model for dry and wet concrete. Through conducting single-element tests, the stress-strain relations predicted by the proposed model under uniaxial tension, uniaxial compression, and triaxial compression were obtained to validate these calibrated parameters. Fig. 8(a) presents a sketch of the single-element test, which brings uniaxial compressive or tensile displacement to bear on a cube element with an edge length of 10 mm to simulate the uniaxial compression or tension test. It further applies the confining pressures on the side surfaces of the cube element in the triaxial compression test. The

compressive stress-strain relation of the 30-MPa dry and wet concrete was obtained using the empirical formula suggested by Attard and Setunge (1996). Fig. 8(b) shows the predictions of the compressive stress-strain relation and shows that the proposed model agrees well with the empirical formula. Fig. 8(c) illustrates the stress-strain relations of dry and wet concrete under dynamic loading. The quasi-static tensile strength of dry concrete was evaluated by the CEB-FIP Model code (Comite Euro-International Du Beton, 1993), i.e., f_t=2.9 MPa for the 30-MPa dry concrete. Compared to dry concrete, wet concrete has a lower dynamic tensile strength at a strain rate of 1 s^{-1} due to its lower quasi-static tensile strength (Zhao and Wen, 2018). However, it has a higher dynamic tensile strength at higher strain rates because of its more significant strain rate effect. Fig. 8(d) illustrates the triaxial compressive stress-strain relations of dry and wet concrete at a confining pressure of 400 MPa. The proposed model and experimental observations of Malecot et al. (2019) show good consistency. In general, the above single-element tests strongly validate the applicability of the calibrated parameters in reproducing the mechanical properties of dry and wet concrete under high pressure and strain rate loadings.

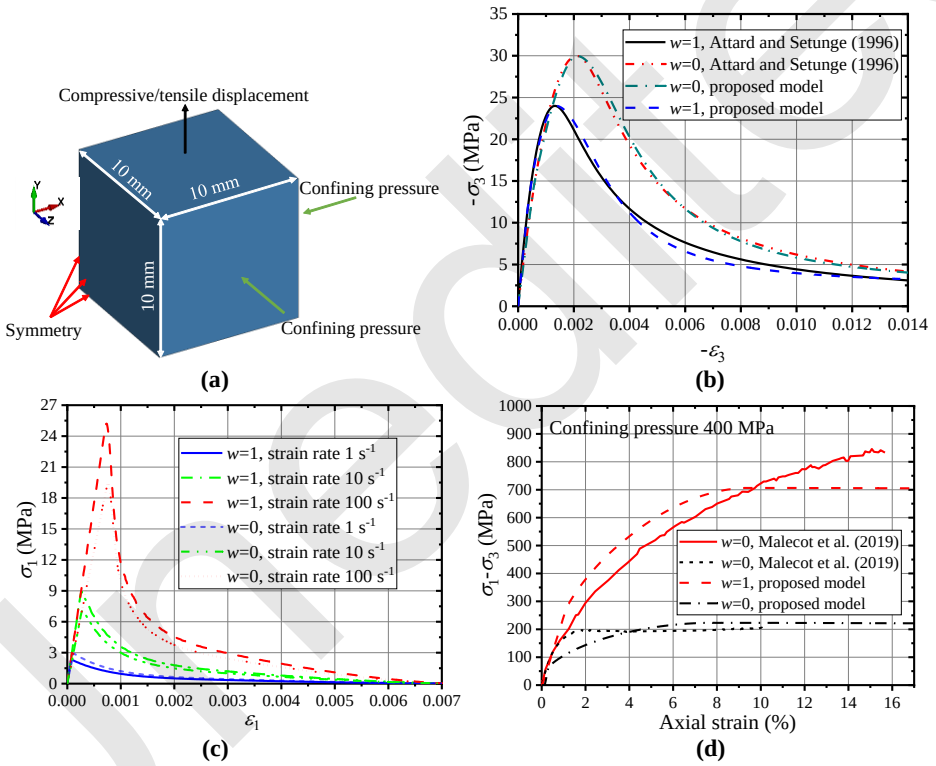

Fig. 8 Comparisons (a) single-element test (b) uniaxial tension (c) uniaxial compression (d) triaxial compression

Table 1 Parameters of the proposed model for dry concrete (w=0)

Basic		f_c, $f_t=0.3f_c^{0.67}$, ρ, $E=4730f_c^{0.5}$, v=0.2, $G=E/2(1+v)$, $K=E/3(1-2v)$									
Strength surface		S_{max}=2600 MPa, $P_0=-0.33f_c$, $f_{bc}=1.25f_c$									
Strain rate effect		W_x=1.75, S=1.1, F_m=10, W_y=5.5, w=0									
Damage function		m=0, A=1.05, d_2=1, $d_1^h=0.0001(5-f_c/20\ \text{MPa})$, $d_1^s=0.08(f_c/\text{MPa})^{-1.33}$, ε_{frac}=0.007									
EOS	μ_1–μ_{10}	0	0.0015	0.0043	0.0101	0.0305	0.0513	0.0726	0.0943	0.174	0.208
	P_1–P_{10}	0	μ_2K	$2\mu_2K$	$3.5\mu_2K$	$8\mu_2K$	$14\mu_2K$	$20\mu_2K$	$28\mu_2K$	$127\mu_2K$	$195\mu_2K$
	$K_{u,1}$–$K_{u,10}$	K	K	1.014K	1.065K	1.267K	1.47K	1.672K	1.825K	4.107K	5K

Table 2 Parameters of the proposed model for wet concrete (w=1)

Basic	$f_c^w=0.8f_c$, $f_t^w=0.8f_t$, ρ, $E^w=1.35E$, v=0.2, $G=E^w/2(1+v)$, $K=E^w/3(1-2v)$
Strength surface	$S_{max}^w=9.2f_c$, $P_0^w=-0.08f_c$, $f_{bc}^w=1.45\ f_c^w$

Strain rate effect		W_x=1.75, S=1.1, F_m=10, W_y=5.5, w=1									
Damage function		m=0, A=1.1, d_2=1, d_1^h=0.0001(5–f_c/20MPa), d_1^s=0.08(f_c/MPa)$^{-1.33}$, ε_{frac}=0.007									
	μ_1–μ_{10}	0	0.0015	0.0043	0.0101	0.0305	0.0513	0.0726	0.0943	0.174	0.208
EOS	P_1–P_{10}	0	μ_2K	1.4μ_2K	2.2μ_2K	5.5μ_2K	11μ_2K	21μ_2K	33μ_2K	127μ_2K	195μ_2K
	$K_{u,1}$–$K_{u,10}$	K	K	1.014K	1.065K	1.267K	1.47K	1.672K	1.825K	4.107K	5K

3 High-fidelity FEA approach and validation

Using the ALE algorithm in the commercial hydrocode LS-DYNA, in this section we establish the high-fidelity FEA approach of the RC slab under a UWCI explosion. Except for the concrete introduced above, the material models of the essential components in the FEA, i.e., the steel reinforcement, water, air, and explosive, are introduced first. Then, the UWCI explosion test on the RC orifice target and the underwater contact explosion test on the saturated concrete slab are simulated to validate the reliability of the FEA approach.

3.1 Material models

3.1.1 Steel

The *MAT_PLASTIC_KINEMATIC model that can consider the isotropic/kinematic hardening effect was used to simulate the steel reinforcement or the steel frame. It describes the strain rate effect using the Cowper-Symonds model, as given in Eq. (11), where C and P are the strain rate parameters, and $\dot{\varepsilon}$ is the strain rate. Table 3 lists the parameters of the steel (Zhou et al., 2023b).

$$\mathrm{DIF}=1+\left(\dot{\varepsilon}/C\right)^{1/P} \tag{11}$$

3.1.2 Explosives

The high energy combustion (CJ) model, i.e., the *MAT_HIGH_EXPLOSIVE_BURN, combined with the Jones-Wilkens-lee (JWL) EOS was adopted to simulate the detonation process of the explosive. The pressure in the explosive element was determined by Eq. (12), where F is the burn fraction, p_{EOS} is the shock wave pressure obtained from the EOS, V is the relative volume, E is the initial internal energy in unit volume, A, B, R_1, R_2, and ω are the EOS coefficients. Table 4 lists the parameters of the TNT (Xu et al., 2022) and emulsion explosives (Yang et al., 2023b). The time and location of the detonation point are defined by *INITIAL_DETONATION.

$$p=Fp_{\mathrm{EOS}}\left(V,E\right) \tag{12a}$$

$$p_{\mathrm{EOS}}=A\left(1-\frac{\omega}{R_1V}\right)e^{-R_1V}+B\left(1-\frac{\omega}{R_2V}\right)e^{-R_2V}+\frac{\omega E}{V} \tag{12b}$$

3.1.3 Air

The air was simulated as a non-viscous ideal gas with no shear strength. The model adopts *MAT_NULL to describe the basic property of air, i.e., the density. The air pressure is accounted for by the *EOS_LINEAR_POLYNOMIAL given in Eq. (13), where E is the initial internal energy per unit volume, μ is the volumetric strain, and C_0-C_6 are the EOS coefficients. Table 5 presents the material parameters of the air (Xu et al., 2022).

$$P=C_0+C_1\mu+C_2\mu^2+C_3\mu^3+\left(C_4+C_5\mu+C_6\mu^2\right)E \tag{13}$$

3.1.4 Water

*MAT_NULL and *EOS_GRUNEISEN were adopted to simulate the water. The pressure in water is determined by Eq. (14a) in the compressed state and Eq. (14b) in the expanded state, which is related to the function of the shock velocity-particle velocity, i.e., $v_s(v_p)$. The parameter C is the intercept of the $v_s(v_p)$ function, S_1, S_2, and S_3 are the coefficients of the slope of the $v_s(v_p)$ function, γ_0 is the Gruneisen gamma, a is the volume correction to γ_0, and E is the initial internal energy per unit volume. The material parameters of the water are listed in Table 6 (Song et al., 2017).

$$P=\frac{\rho_0C^2\mu\left[1+\left(1-\gamma_0/2\right)\mu-a\mu^2/2\right]}{\left[1-\left(S_1-1\right)\mu-S_2\,\mu^2/\left(1+\mu\right)-S_3\,\mu^3/\left(1+\mu\right)^2\right]^2}+\left(\gamma_0+a\mu\right)E \tag{14a}$$

$$P=\rho_0C^2\mu+\left(\gamma_0+a\mu\right)E \tag{14b}$$

Table 3 Plastic kinematic model parameters of the steel (Zhou et al., 2023b)

ρ (kg/m^3)	E (GPa)	v	Yield strength (MPa)	E_t (GPa)	C (s^{-1})	P	Failure strain
7800	210	0.3	400/235	2	40	5	0.14

Table 4 CJ model and JWL EOS parameters for the explosives

Explosives	ρ (kg/m^3)	D (m/s)	P_{cj} (GPa)	A (GPa)	B (GPa)	R_1	R_2	ω	E_0 (J/m^3)
TNT	1630	6930	21	373.8	3.747	4.15	0.9	0.35	6×10^9
Emulsion	1150	5500	7.4	214.4	0.182	4.2	0.9	0.15	4.2×10^9

Table 5 *MAT_NULL and *EOS_LINEAR_POLYNOMIAL parameters for the air (Xu et al., 2022)

ρ (kg/m^3)	E (MPa)	Pressure cutoff	C_0	C_1	C_2	C_3	C_4	C_5	C_6
1.29	0.25	0	0	0	0	0	0.4	0.4	0.6

Table 6 *MAT_NULL and *EOS_GRUNEISEN parameters for the water (Song et al., 2017)

ρ_0 (kg/m^3)	E (MPa)	S_1	S_2	S_3	γ_0	a	C (m/s)
1020	0	1.92	–0.096	0	0.25	0	1650

3.2 UWCI explosion test on RC orifice targets

Yang et al. (2023b) conducted a UWCI explosion test on two RC orifice targets, denoted T1 and T2, inside a water tank with dimensions of ϕ2000×2000 mm. Fig. 9 presents the scheme of the UWCI explosion test. The emulsion explosive weighed 7 g and was detonated by a high energy pulse detonator containing nearly 1 g emulsion explosive at the center of the entrance to the orifice. The RC orifice target had dimensions of 400×400×200 mm and was supported by a steel frame. A pressure sensor was installed in the water to measure the pressure-time history. The position of the sensor is illustrated in Fig. 9(b).

(a)

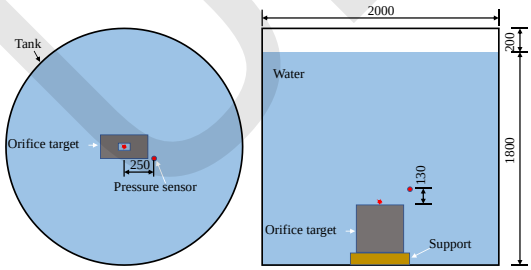

(b)

Fig. 9 Scheme of the UWCI explosion test: (a) photograph (Yang et al., 2023b) (b) test setup (unit: mm)

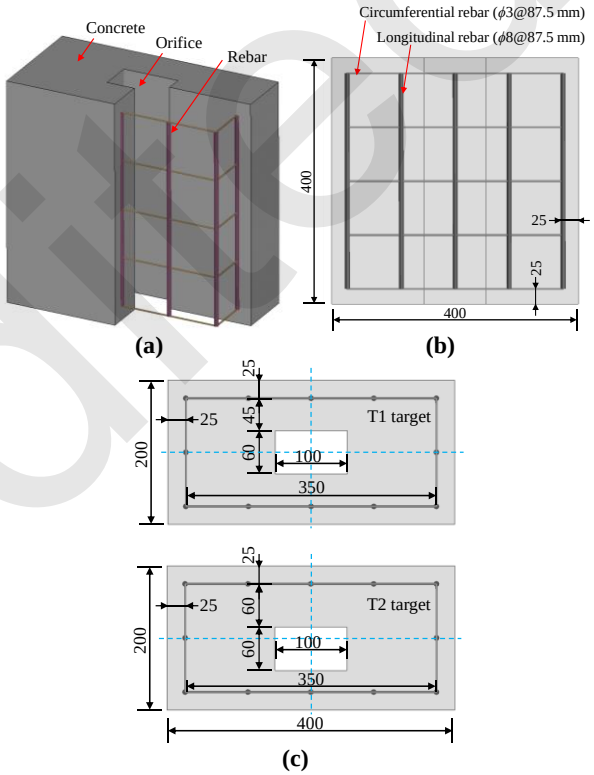

Fig. 10 Dimensions of the RC orifice targets (unit: mm): (a) sketch map (b) side view (c) top view

Fig. 10 details the dimensions and reinforcement setting of the T1 and T2 targets. The orifices in the two targets had dimensions of 400×100×60 mm and different axis positions (Figs. 10(b)). The concrete had a compressive strength of 37 MPa. The steel reinforcement along the longitudinal and circumferential directions had a yield strength of 400 MPa and 235 MPa, respectively.

Fig. 11 presents the finite element model of this UWCI explosion test. A 1D beam element was applied to discrete the steel rebar, and a 3D solid element was adopted to model the other components, including the concrete, support, water, and emulsion

explosive. The mesh sizes of the concrete, steel rebar, and support were 5 mm, 10 mm, and 15 mm, respectively. The material failure of the concrete was defined by *MAT_ADD_EROSION, which was set at the maximum principal strain of 0.075. It uses the *CONSTRAINED_LAGRANGE_IN_SOLID keyword to couple the steel rebar and concrete target, as well as to make the Euler mesh and Lagrange mesh work together. The interaction between the RC orifice target and the steel support was defined by the *CONTACT_AUTOMATIC_SURFACE_TO_SURFACE algorithm. The bottom of the steel support was the fixed boundary. A water region with dimensions of 800×400×200 mm was built, the top and side surfaces of which were set as the non-reflecting boundary. The emulsion explosive was generated in the water using the volume-filling command of *INITIAL_VOLUME_FRACTION_GEOMETRY.

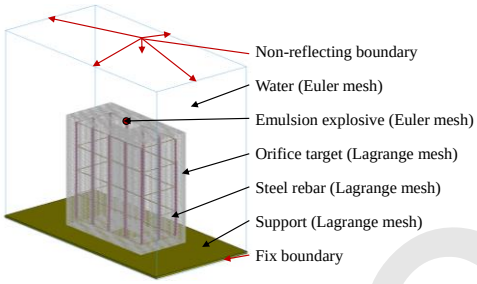

Fig. 11 Finite element model of the UWCI explosion test on the RC orifice target

The simulated pressure-time history in water is affected by the mesh size of the water. Therefore, a sensitivity analysis was conducted on the mesh size to precisely reproduce the underwater explosion load. Fig. 12 shows comparisons of the pressure-time history in the water between test data (Yang et al., 2023b) and simulation results. The peak pressure of the shock wave in water rises as the mesh size is reduced. When the mesh size of water was set as 11.5 mm, the simulation result agreed well with the corresponding experimental observation. Therefore, the 11.5 mm mesh size of water was adopted.

A rational terminal time needs to be determined to improve the computing efficiency. According to Cole (1948), an underwater explosion load includes a shock wave and bubble pulse. The shock wave has a short duration of <1 ms (Fig. 12), while the duration of the bubble pulse is over one hundred times longer. For an underwater contact explosion scenario, Wen et al. (2023) found that the shock wave is mainly responsible for the damage to the concrete, while the bubble pulse has a negligible effect. Thus, only the damage caused by the shock wave was simulated in this study, to save computing time. Fig. 13 presents the evolution of the total damage (D) to the T1 target, indicating that the damage pattern becomes convergent after a detonation time of 6.4 ms. Hence, the convergent simulation results at a compute time of 10 m are presented in this section.

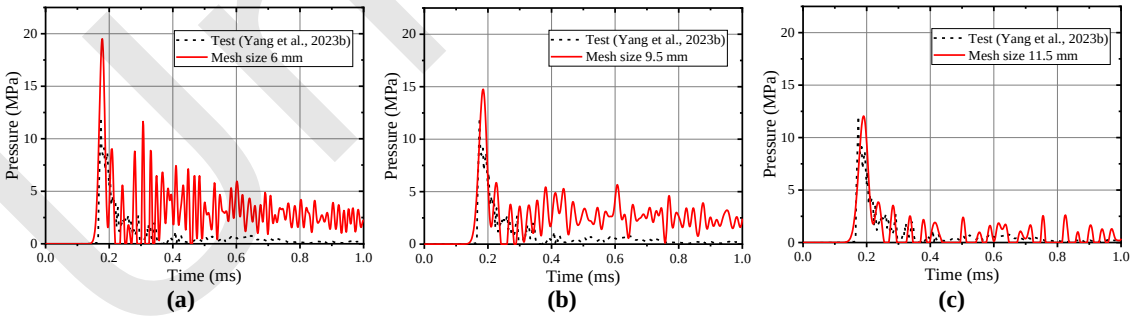

Fig. 12 Predictions of pressure time histories in water with a mesh size of (a) 6 mm (b) 9.5 mm (c) 11.5 mm

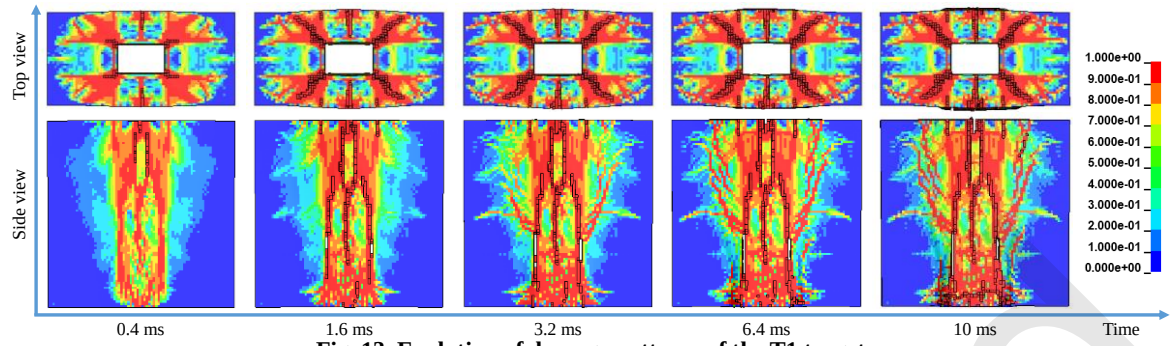

Fig. 13 Evolution of damage patterns of the T1 target

Fig. 14 compares the total damage patterns of RC orifice targets between simulations and tests. The test photographs (Yang et al., 2023b) show that the extent of damage to the T1 target is severe near the detonation point, i.e., the center of the orifice on the top surface. In the top view, three main radial cracks crossing through each outer long edge surface to the internal orifice surface appear in the T1 target. There are also many macro cracks between the main cracks. In the side view, these three main cracks develop down from the top surface, while only the main crack near the symmetric line propagates to the bottom surface. The T2 target has almost an identical damage pattern while being unsymmetric in distribution due to the different position of the orifice. Specifically, the T2 target showed a greater extent of damage on the weak sides than on the strong sides. The simulation results show that the failure patterns of the T1 and T2 targets on the top and side surfaces are precisely reproduced by the established FEA approach. Near the corner between the long edge surface and the top surface, the distances between the main cracks were 321/341 mm on the two sides of the T1 target and 255/310 mm on the strong and weak sides of the T2 targets. The corresponding simulation results of the T1 and T2 targets were 315/316 mm and 266/299 mm, respectively, which are within a deviation of 7%.

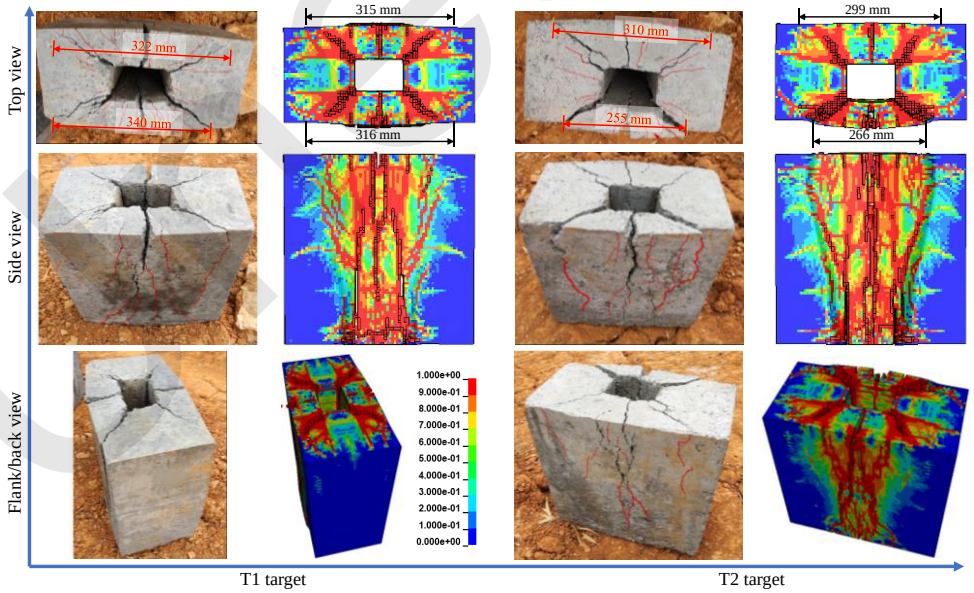

Fig. 14 Comparisons of damage patterns of orifice targets between simulations and tests (Yang et al., 2023b)

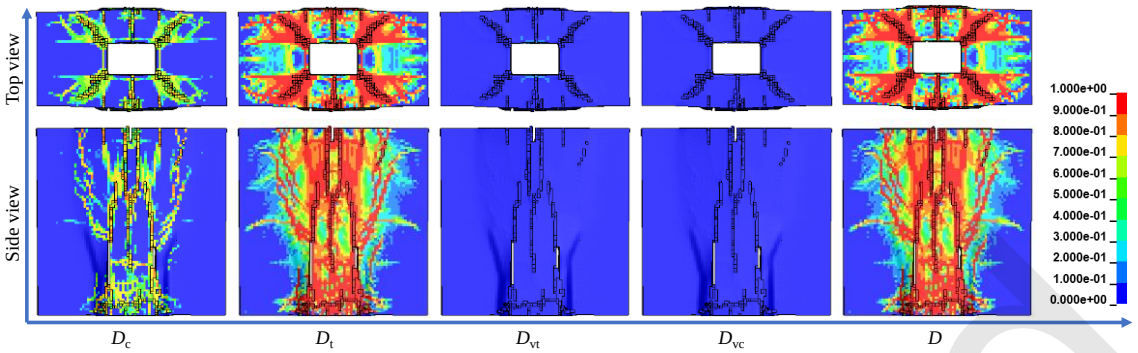

Fig. 15 Predicted damage variables of the T1 target under a UWCI explosion

Fig. 15 presents the predicted compressive (D_c), tensile (D_t), volumetric compressive (D_{vc}), volumetric tensile (D_{vt}), and total (D) damage of the T1 target. The compressive and tensile damage caused by the shear deformation dominates the failure of the T1 target under the UWCI explosion. Comparatively, the damage caused by volumetric compaction had a negligible effect since the peak pressure of the shock wave decreased rapidly with increasing distance, and the stress state of the concrete material did not lie in hydrostatic compression. Besides, the tensile damage was much more severe than the compressive damage, and the tensile damage pattern was almost the same as the total damage pattern. Therefore, the failure of the RC orifice under a UWCI explosion is affected mainly by the mechanical properties of the concrete material in the low-pressure range, especially the tensile property. Thus, improving the dynamic tensile property of the concrete material could effectively enhance its resistance against the UWCI explosion, which agrees with the findings of Yang et al. (2023b).

3.3 Underwater contact explosion test on saturated concrete slabs

Wen et al. (2023) conducted underwater contact explosion tests on saturated concrete slabs using explosives with equivalent TNT masses of 2.5, 5, and 10 g. Fig. 16 presents the test setup and corresponding finite element model, where the concrete slab had dimensions of ϕ400×80 mm and was placed on a steel frame. The compressive strength of the concrete measured by the 150-mm edge length cubic specimens was 44 MPa. During the test, the detonator, cylinder TNT explosive, and booster explosive were assembled by the waterproof tap and detonated at the center of the saturated concrete slab to generate the underwater blast loading. In the finite element model, a TNT explosive cylinder with a length-to-diameter ratio of 1 was built. The mesh size, material failure criterion, boundary conditions, contact type, and coupling algorithm were identical to those in Section 3.2.

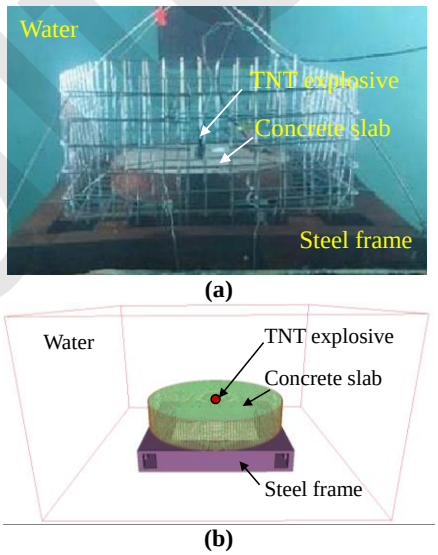

Fig. 16 Underwater contact explosion test: (a) test setup (Wen et al., 2023) (b) finite element model

Fig. 17 compares the damage patterns of the saturated concrete slabs between experimental observations (Wen et al., 2023) and simulation results. The test photographs show that the saturated concrete slabs had a spall failure mode in the 2.5-g TNT test scenario and breach failure mode in the 5-g and 10-g TNT test scenarios. A circle crater with a relatively small diameter appeared in the front surface, while the spall with an obviously larger diameter was accompanied by many radial cracks on the rear surface. The dimensions of both the crater and spall increased with increasing mass of TNT. The simulated failure modes of the saturated concrete panel under the three

test scenarios agreed with corresponding experimental observations (Fig. 17). Table 7 compares the failures of the saturated concrete slabs between test data (Wen et al., 2023) and simulation results. The simulation results of the crater and spall diameters in the 5-g and 10-g TNT test scenarios were within the corresponding measurement range (Fig. 17 and Table 7). However, there was an apparent deviation between the simulation result and test data in the 2.5-g TNT test scenario, which could have been caused by the difference in the explosive between the finite element model and the field test. Apart from the TNT explosive cylinder, in the field test the explosive contained a detonator and booster explosive, the equivalent TNT mass and shape of which affected the failures of the saturated concrete slab when the mass of the cylinder TNT explosive was low, i.e., in the 2.5-g TNT test scenario. Hence, the established FEA approach could reasonably reproduce the damage patterns of the saturated concrete slabs subjected to underwater contact explosions.

To illustrate the damage mechanism of the saturated concrete slab, Fig. 18 presents the predicted D_c, D_t, D_{vc}, D_{vt}, and D in the 10-g TNT test scenario. The volumetric damage (D_{vc}, D_{vt}) was minor and concentrated near the center of the front surface. The reason is that only the concrete near the explosive suffered from the significant shock wave pressure. The rear part of the saturated concrete slab experienced a smaller shock wave pressure or did not lie in the hydrostatic compaction state. In contrast, the shear damage (D_c, D_t) was prominent and had a larger extent of distribution near the rear surface since the shear deformation was larger than the volumetric compaction deformation. The tensile damage D_t had a larger distribution area and greater extent than the D_c, because the concrete becomes fragile as the pressure decreases. Combined with Figs. 15 and 18, we conclude that the failure of concrete structures under a UWCI explosion is inherently caused by the tensile damage, even for those materials adjacent to the detonation point.

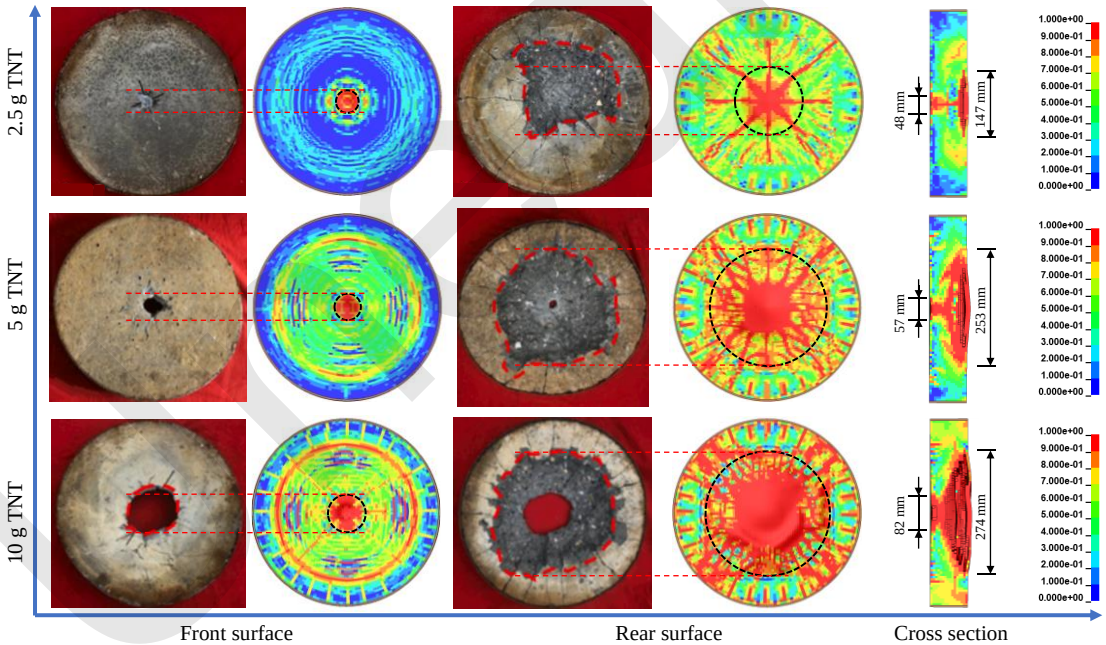

Fig. 17 Comparisons between experimental observations (Wen et al., 2023) and simulation results

Table 7 Failures of saturated concrete slab subjected to an underwater contact explosion

Equivalent TNT mass (g)	Crater diameter (mm)		Spall diameter (mm)	
	Wen et al. (2023)	Simulation	Wen et al. (2023)	Simulation
2.5	17–35	48	160–286	147
5	23–59	57	245–314	253
10	81–121	82	255–324	274

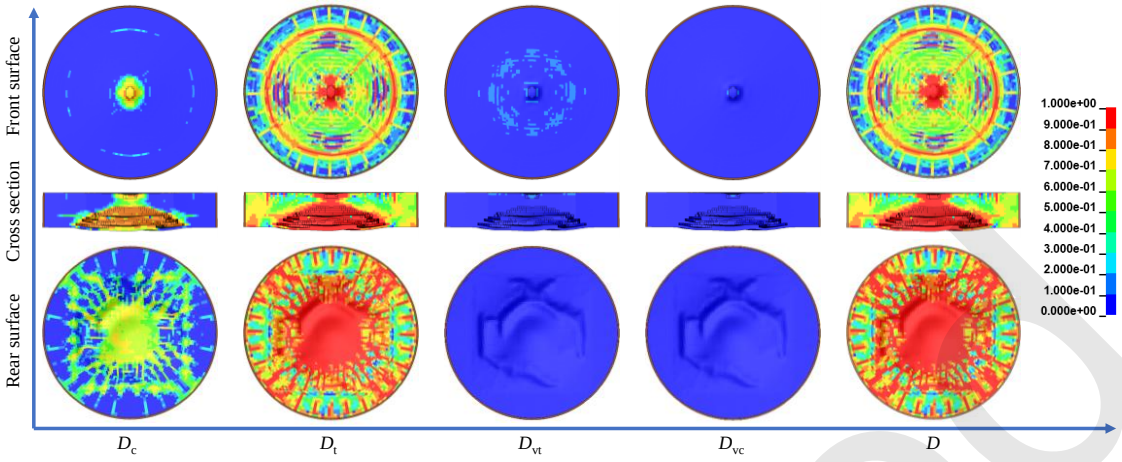

Fig. 18 Predicted damage variables of the saturated concrete slab in the 10-g TNT test scenario

4 RC slab under a UWCI explosion

Adopting the FEA approach validated above, in this section we further design an RC slab and evaluates its performance under a UWCI explosion. We also examine the effect of some critical parameters, including the charge weight (W), standoff distance (R), structural thickness (T), and water/air-back conditions, on the damage patterns of the RC slab. The typical failure modes, i.e., no spall, spall (no breach), and breach, are numerically reproduced. Based on extensive simulations, we propose an empirical formula to predict the failure modes of an RC slab under a UWCI explosion.

4.1 Case design

In the baseline UWCI explosion case, a TNT explosive cylinder with a mass of 200 g is detonated 100 mm away from the center of an RC slab with dimensions 3000×3000×160 mm. The concrete has a compressive strength of 40 MPa and the corresponding f_c^w=32 MPa. The TNT explosive has a length-to-diameter ratio of 1, and the detonation point is in the center. Hence, the scaled distance $Z=R/W^{1/3}$ and scaled thickness $H=T/W^{1/3}$ of the baseline case are Z=0.171 and H=0.274, respectively. Fig. 19 presents the steel reinforcement distribution in the RC slab and a sketch map of the close-in explosion scenario. The radius of the TNT explosive is r and the standoff distance is R. The distance between the RC slab's top surface and the TNT's rear surface, denoted s, has $s=R–r$. A steel reinforcement with a yield strength of 400 MPa and spacing of 200 mm was adopted and the concrete cover thickness was 25 mm.

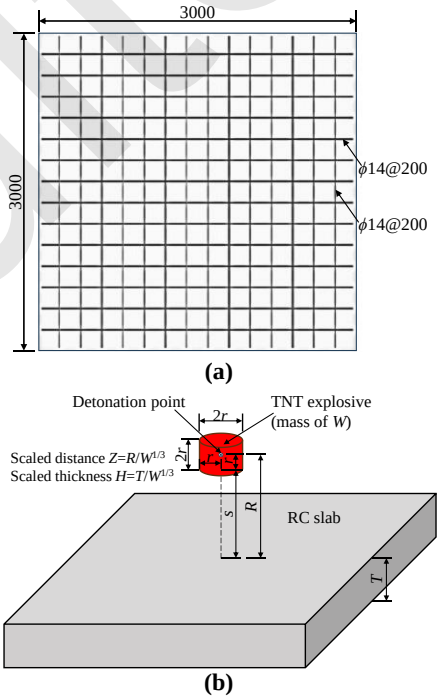

Fig. 19 The RC slab under a UWCI explosion: (a) RC slab dimensions (unit: mm) (b) scheme of close-in explosion

Fig. 20 presents the finite element model of the baseline UWCI explosion scenario. Considering the symmetry of the scenario, a 1/4 finite element model was built to improve computing efficiency. The 1/4 Euler mesh region had dimensions of 1590×1590×1200 mm. The boundaries of the Euler mesh region, except for the symmetry plane, were set as the non-reflecting boundary. An elastic frame was adopted to provide enough constraint to the concrete

slab. It was described by *MAT_ELASTIC and had the same density, elastic modulus, and Poisson's ratio as the concrete. The RC slab shared the same mesh nodes as the elastic frame at their boundary. The upper and lower surfaces of the elastic frame were set as the fixed boundary. Six displacement measurement points in the front and rear surfaces of the RC slab, shown as red points in Fig. 20(b), were selected to assess the structural response. In addition, two blue points in water/air were adopted to record the shock wave on the incident and distal sides of the RC slab 10 mm from the front and rear surfaces, respectively.

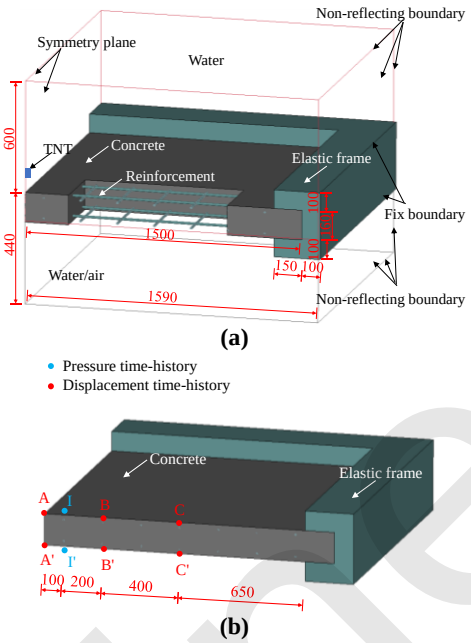

Fig. 20 Baseline UWCI explosion scenario (unit: mm): (a) finite element model (b) measurement points

Fig. 21 presents the simulation results of the baseline UWCI explosion scenario after a detonation time of 30 ms, which is a breach failure mode. The cross section in Fig. 21(a) shows that the material failure is concentrated in the center of the RC slab where the crater and spall connect with each other. The diameters of the crater and spall (880 mm and 870 mm) are about the same, while the height of the spall is larger than that of the crater (100 mm vs. 60 mm). There are also hoop and radial cracks on the front and rear surfaces, respectively, dominated by different deformation forms. The UWCI explosion caused vertical and radical deformation on the RC slab, from compression and tension near the front and rear surfaces. Near the front surface, the RC slab deformed like a cantilever beam bending towards the rear surface direction, causing the hoop cracks to appear on the extension side. Near the rear surface, the vertical and radical tension deformation resulted in radical cracks. Cracks tended to develop along the steel reinforcement near the rear surface due to the interaction between the steel reinforcement and the concrete (Zhou et al., 2023b). In addition, there was a vertical crack near the boundary between the RC slab and the elastic frame caused by the strain localization.

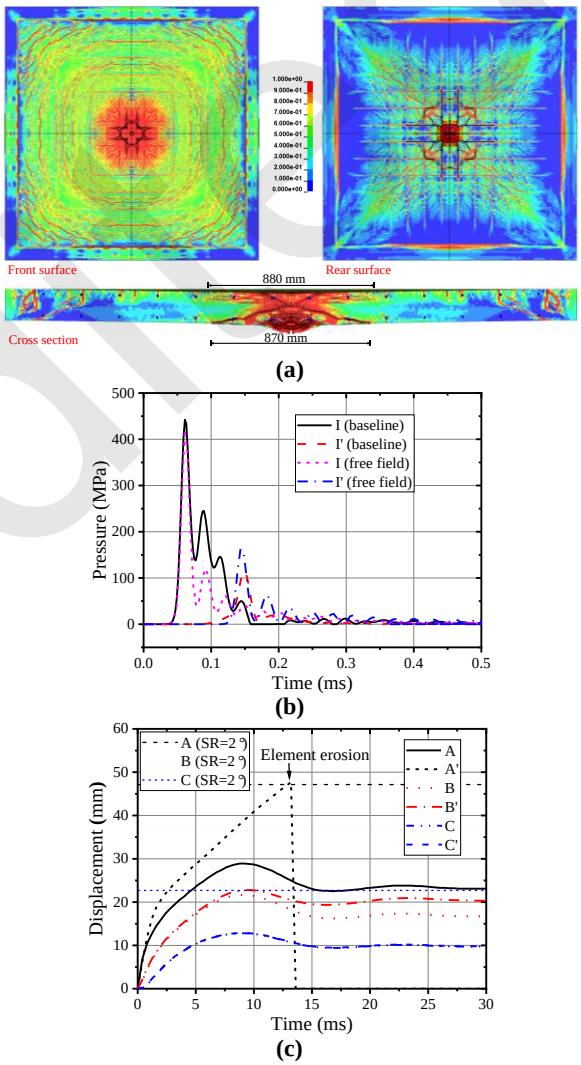

Fig. 21 Simulation results of the baseline scenario: (a) damage pattern (b) shock wave (c) structural response

Fig. 21(b) shows the pressure time histories of points I and I' and the corresponding simulation results in the free field underwater explosion for comparison. At point I, the pressure decreases rapidly after reaching the peak pressure under the free field

explosion, while it has several minor peak pressures after the peak in the baseline explosion scenario because of the reflection of the shock wave near the incident surface. The comparison of the pressure time histories at point I' shows that the RC slab alleviates the peak pressure near the distal surface, i.e., the pressure drops from 162 MPa to 114 MPa. Fig. 21(c) shows the structural response of the RC slab, where the displacements of the measurement points reach the peak value at nearly 10 ms and reduce to a residual value after 15 ms. Note that the concrete element at point A' is eroded at 13.6 ms. The peak displacement increases as the measurement points come close to the center of the RC slab. The local material failure would cause a difference in the displacement between the front and rear surfaces. Thus, the increasingly apparent difference in displacement from points C/C' to A/A' means there is a strongly localized failure pattern in the RC slab center, which agrees with that presented in Fig. 21(a). The structural failure mode was assessed by the support rotation (SR). Chen et al. (2023) defined SR<2 °, 2 °<SR<6 °, and 6 °<SR<12 °as the slight, medium, and severe structural failure modes, respectively, for an RC slab. The SRs obtained from these measurement points, except for point A' in the spall, are within 2 °; hence, the structural failure is slight.

4.2 Parametric studies

Fig. 19(b) shows that the failure mode of the RC slab depends on *W*, *R*, and *T* when the material properties are unchanged. The Euler mesh region illustrated in Fig. 20 on the incident side is water since the UWCI explosion was assumed to come from the outside. However, the water or air could be on the distal side to simulate different underwater facilities, such as a tunnel or caisson wharf. Thus, parametric studies of the four parameters, *W*, *R*, *T*, and the air/water-back conditions, were conducted as follows.

4.2.1 Charge weight

The effect of the charge weight was examined by changing *W* to 25, 50, or 100 g based on the baseline UWCI explosion scenario (*W*=200 g). Fig. 22 presents the corresponding damage patterns of saturated RC slabs. The cratering and hoop cracking near the front surface, as well as the spalling and radical cracking near the rear surface, become severe with increased charge weight due to the absorption of more detonation energy. As the local failure becomes more severe, the RC slab exhibits two typical failure modes: the spall failure mode in the *W*=25 g, 50 g, and 100 g scenarios and the breach failure mode in the *W*=200 g scenario. Damage accumulated more easily on the rear surface than on the front surface. Specifically, hoop cracks were relatively insignificant in contrast to radical cracks in the *W*=25 g and 50 g scenarios, and the spalling started to generate at a lower charge weight than the cratering, i.e., 50 g vs. 100 g. The reason is that the propagation of shock waves causes compression stress near the front surface and is reflected as tensile stress near the rear surface, and the material failure is dominated by the tensile damage, as identified in Section 3.

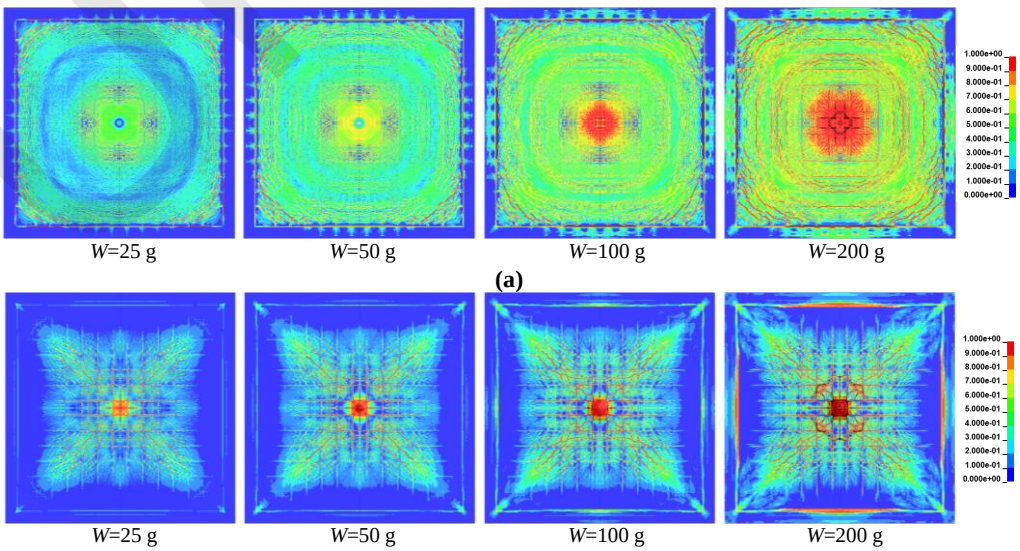

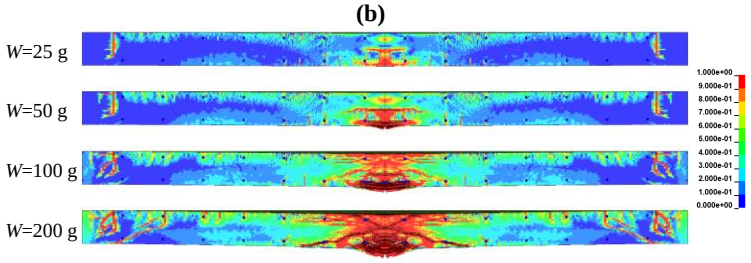

Fig. 22 Effect of charge weight on damage patterns: (a) front surface (b) rear surface (c) cross section

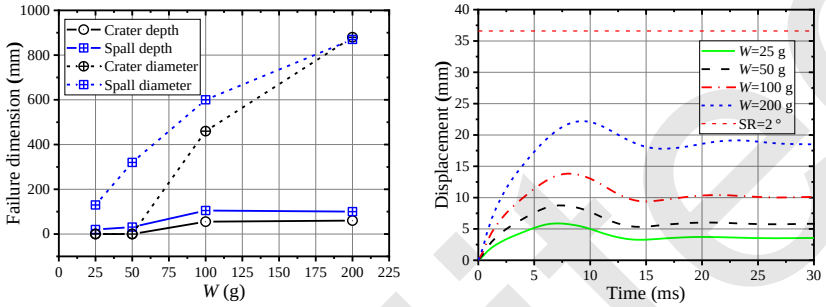

Fig. 23 Effect of charge weight on the (a) failure dimension (b) structural response

Fig. 23 further illustrates the effect of charge weight on the local failure dimension and structural response of the saturated RC slab. The average structural displacements at points B and B' with various charge weights are given in Fig. 23(b). The diameters and depths of the crater and spall increase with the charge weight. The spall has larger dimensions than the crater in the same UWCI explosion scenario. The peak displacement increases with charge weight, and the four scenarios show slight structural damage. Therefore, the local material failure, instead of the structural failure, is critical to the engineering design of a water-backed RC slab against a UWCI explosion.

4.2.2 Standoff distance

Based on the baseline UWCI explosion scenario (R=100 mm), the standoff distance R was changed to 50, 200, and 400 mm, respectively. Fig. 24 presents comparisons of the damage patterns of RC slabs (cross section) under UWCI explosions at different standoff distances.

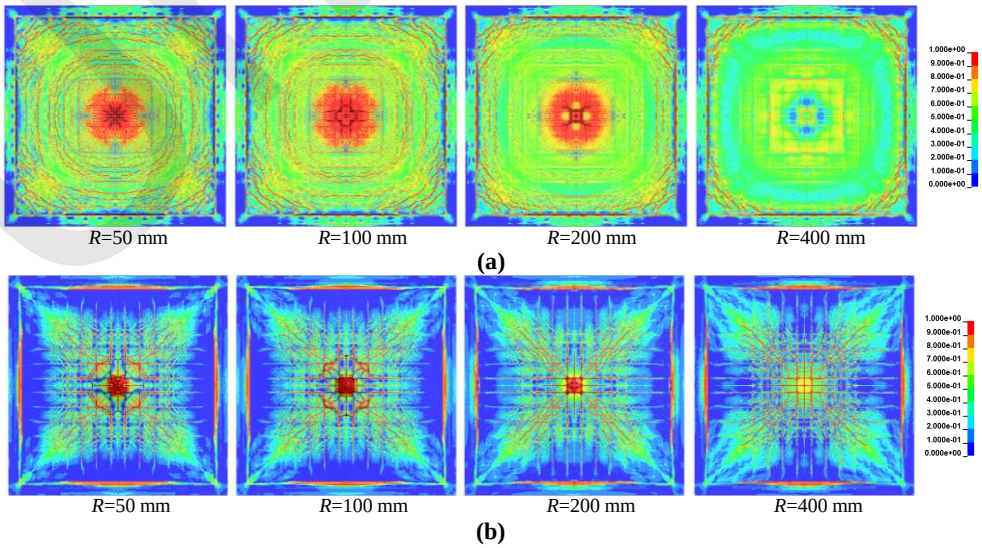

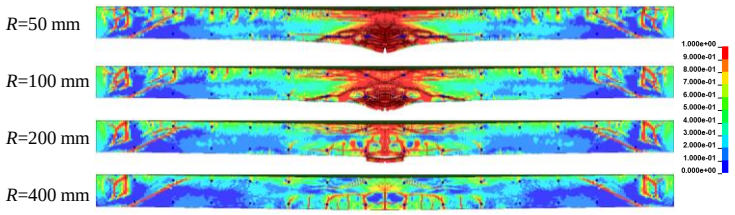

(c)

Fig. 24 Effect of standoff distance on damage patterns: (a) front surface (b) rear surface (c) cross section

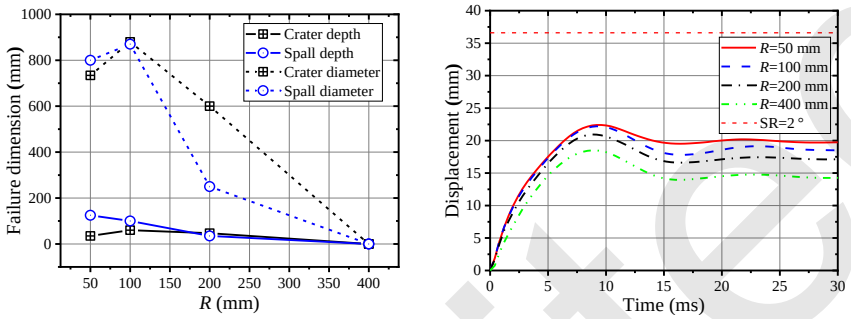

(a) (b)

Fig. 25 Effect of standoff distance on the (a) failure dimension (b) structural response

Fig. 25 gives the corresponding local failure dimensions and structural responses. When the standoff is greater than 100 mm, the front hoop cracking, front cratering, rear spalling, and the structural displacement generally reduce with increasing standoff distance since the shock wave dampens rapidly as the standoff distance increases. The radial cracking on the rear surface is relatively insensitive to the change of standoff distance, and all four slabs have a slight structural failure mode. The R=100 mm, 200 mm, and 400 mm scenarios exhibit three typical failure modes, i.e., the breach, spall, and crack, which could be classified as severe, medium, and slight failure modes. When the standoff distance was less than 100 mm, the RC slab's crater and spall merge, leading to a breach failure mode. Compared to the R=50 mm scenario, the R=100 mm scenario exhibits larger crater and spall dimensions, while the average peak structural responses at points B and B' in the two scenarios are almost the same. This may be caused by the combined effect of the decreased shock wave pressure and increased incident angle. Besides, it also indicates that the local failure would not increase linearly with the reduction of standoff distance within a threshold value, and there exists an optimum destructive standoff distance of a UWCI explosion.

4.2.3 Structural thickness

To study the effect of the structural thickness T, the thickness of the RC slab was adjusted to 120, 200, or 240 mm according to the baseline scenario (T=160 mm). Fig. 26 presents the effect of the structural thickness on the damage pattern, and Fig. 27 shows the corresponding failure dimensions and structural response. The front hoop cracking, front cratering, rear spalling, and structural response reduce with rising structural thickness. Similar to the standoff distance, the structural thickness has a minor influence on the distribution area and extent of the radial cracking on the rear surface. When the structural thickness is less than 160 mm, the front crater and rear spall in the RC slabs remains almost unchanged with a diameter of nearly 860 mm and merged. When the structural thickness increases over 160 mm, the diameters of the crater and spall decrease, i.e., from nearly 860 mm when T=160 mm to 480 mm when T=240 mm, and detach from each other with an increasing distance, leading to the spall failure mode. The average displacements at points B and B' show that the peak displacement and corresponding compute time rise with the reduced structural thickness due to the increased structural stiffness. The RC slabs in the four simulated scenarios have a slight structural failure mode. In summary, this indicates that the anti-explosion performance of underwater facilities can be improved by improving the structural thickness.

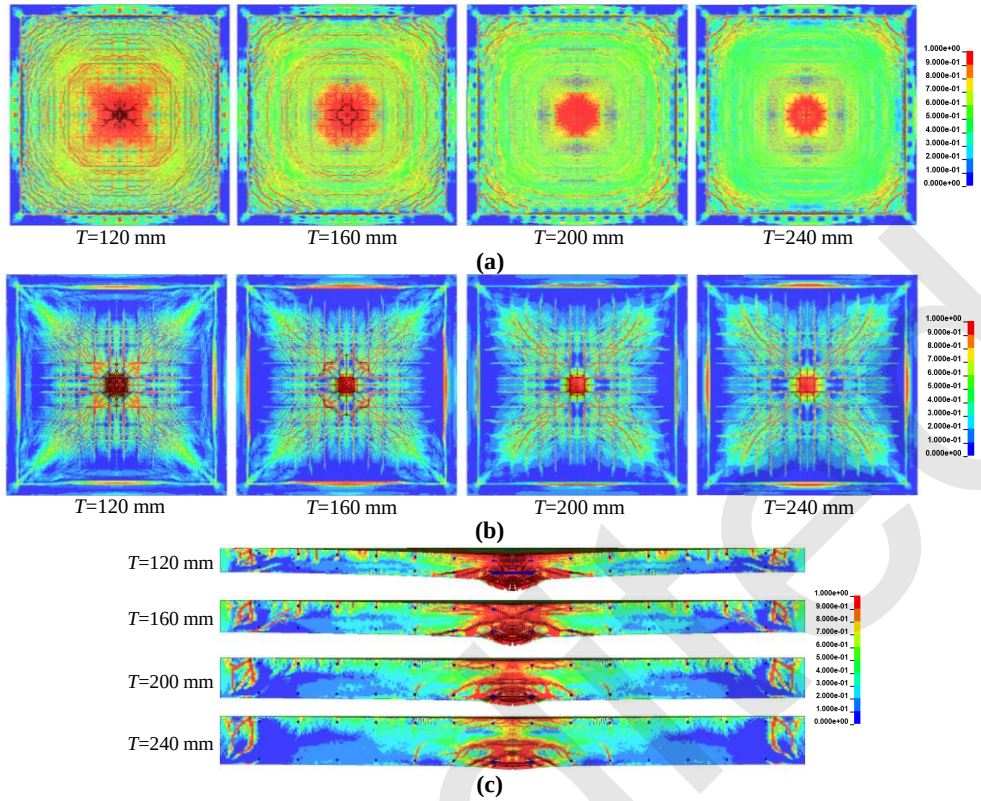

Fig. 26 Effect of structural thickness on damage patterns: (a) front surface (b) rear surface (c) cross section

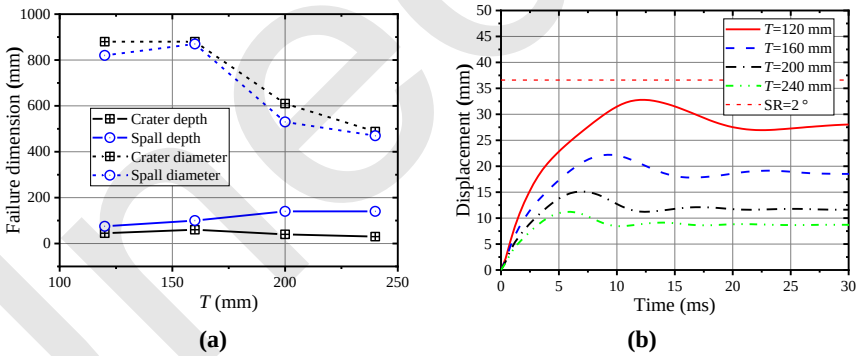

Fig. 27 Effect of structural thickness on the (a) failure dimension (b) structural response

4.2.4 Water/air-back conditions

The water on the distal surface of the RC slab in the baseline UWCI explosion scenario was replaced by air to examine the effect of the water/air-back conditions. Fig. 28 presents comparisons of the damage patterns of water-backed and air-backed slabs. The air-backed slab has local breach failure in the center and structural punch shear failure near the outer boundaries, which is significantly more severe than that of the water-backed slab and coincides with the findings of Yang et al. (2022).

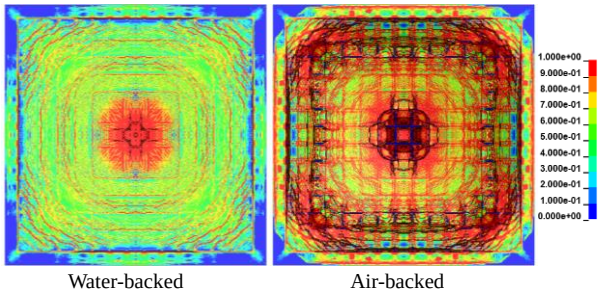

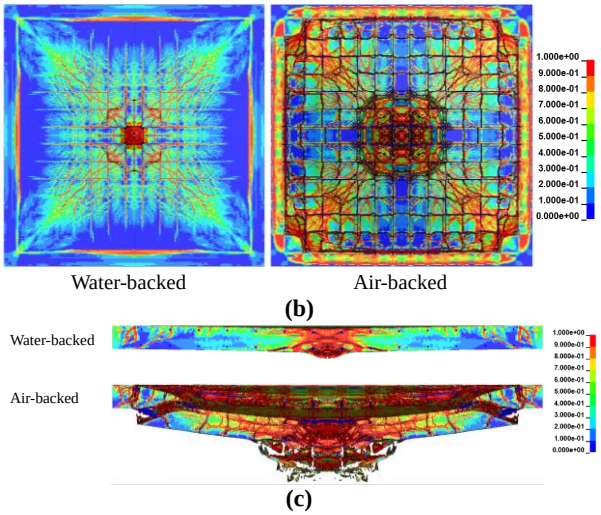

Fig. 28 Effect of water/air-back conditions on damage patterns: (a) front surface (b) rear surface (c) cross section

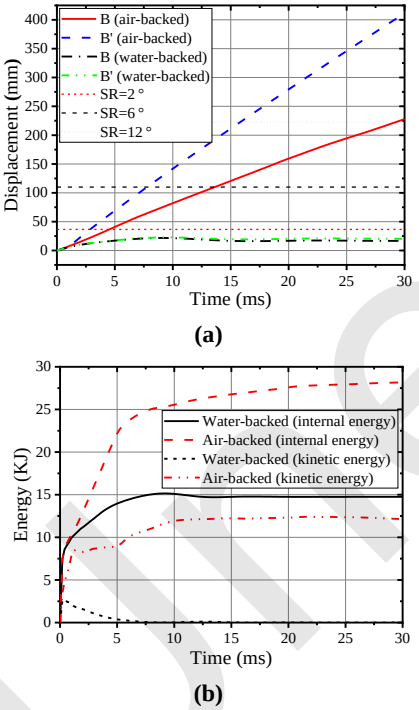

Fig. 29 Effect of water/air-back conditions on (a) the structural response (b) energy

Fig. 29 illustrates the effect of the water/air-back conditions on the structural response and energy time histories of the concrete part. Fig. 29(a) shows that the water-backed RC slab has already converged to the residual displacement, and the structural damage mode is slight. Comparatively, the air-backed RC slab keeps moving away and has a severe structural damage mode, i.e., SR>12 °. The energy of concrete absorbed from the detonation of the TNT charge includes kinetic and internal energy. A larger kinetic energy corresponds to a larger structural velocity response, and a larger internal energy means more severe deformation or material failure. Fig. 29(b) shows the air-backed slab absorbed nearly 1.9 times the internal energy of the water-backed slab, which agrees with the more severe material failure in Fig. 28. Furthermore, the kinetic energy of the air-backed and water-backed slabs retained at 15 KJ and 0 KJ, respectively, corresponding to the convergent and linearly increasing structural displacements in Fig. 29(a), respectively.

To illustrate the significant effect of the water/air-back conditions, Fig. 30 presents the shock wave propagation processes. The shock wave reaches the front and rear RC slab surfaces at nearly 0.04 ms and 0.11 ms, respectively. There is almost no difference in the propagation of the shock wave before it reaches the rear surface. As the shock wave propagates further into the distal side, the shock wave transmitted in the water is significantly larger than that in the air due to the difference in wave impedance between water and air. Specifically, the peak shock wave at the point I' in the water is about 4000 times that in the air, i.e., 118 MPa vs. 0.029 MPa. Compared to the air, the water in the distal surface could transmit a larger shock wave, reduce the reflected tensile shock wave in the RC slab, and thereby alleviate the local and structural failure of the RC slab. Briefly, the medium in the distal surface significantly affects the failure pattern of the RC slab, and the air-backed RC structure is more fragile in response to a UWCI explosion than the water-backed RC structure.

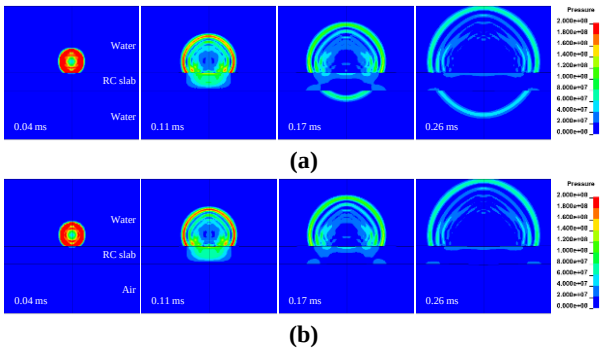

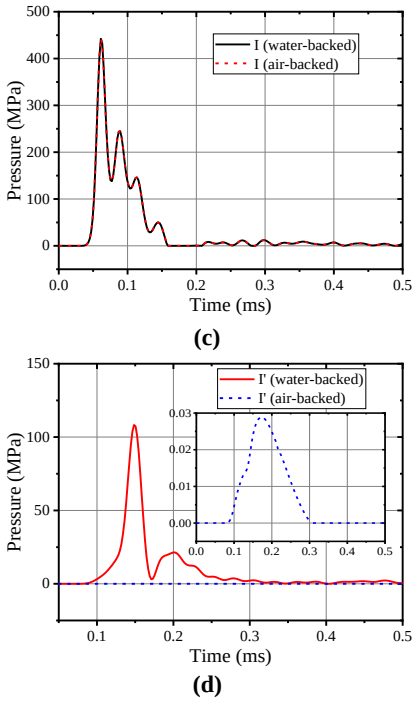

Fig. 30 Effect of water/air-back conditions on the shock wave: (a) water-back scenario (b) air-back scenario (c) incident surface (d) distal surface

4.3 Empirical formulae for predicting failure modes

For the anti-explosion design of underwater structures, it is necessary to predict the damage modes of an RC panel subjected to the UWCI explosion. Based on experimental observations, McVay (1988) summarized empirical formulae to determine the spall and breach limits of RC slabs under in air close-in explosions, which is given in Eq. (15). It assumes that the scaled thickness $H=T/W^{1/3}$ is a function of the scaled distance $Z=R/W^{1/3}$ when the local failure of the RC slab is in the limit states between the no spall, spall, and breach failure modes. Taking the same assumption, in this study we designed over ninety simulation cases by changing the W, R, T, and water/air-back conditions based on the baseline case presented in Section 4.1 to obtain the failure modes of RC slabs under different combinations of Z and H.

$$\text{Spall limit (McVay, 1988):}\ \frac{T}{W^{1/3}}=0.073\left(\frac{R}{W^{1/3}}\right)^{-0.58} \quad (15a)$$

$$\text{Breach limit (McVay, 1988):}\ \frac{T}{W^{1/3}}=0.032\left(\frac{R}{W^{1/3}}\right)^{-0.58} \quad (15b)$$

For the water-backed RC slab, fifty-four simulation results were obtained from RC slabs with 120 mm, 160 mm, and 240 mm thicknesses. Fig. 31(a) presents the designed fifty-four simulation cases, and Fig. 31(b) gives the corresponding simulation results. The failure modes of the water-backed RC slabs with various T, W, and R combinations subjected to UWCI explosions are located in three regions with clear boundaries. Through data fitting, this drives the spall and breach limits of the water-backed RC slab subjected to a UWCI explosion, which are given in Fig. 31(b) and Eq. (16). Compared to the predictions of the Eq. (15) (McVay, 1988), we conclude that the UWCI could cause more severe damage on the RC slab than the in-air close-in explosion. For example, when $R/W^{1/3}$ equals 0.3, the thickness of the water-backed RC slab to avoid the spall and breach failures under UWCI explosion needs to be 2.6 and 3.1 times that under an in-air close-in explosion. The difference would further increase as $R/W^{1/3}$ decreases due to the larger negative exponential coefficients in Eq. (17) than in Eq. (16). In addition, note that the predictions of the spall and breach limits have interaction near $R/W^{1/3}$=0.75, meaning the predictions of when $R/W^{1/3}$>0.75 are unphysical. As the $T/W^{1/3}$ decreases and the $R/W^{1/3}$ increases, the failure mode of the RC slab would gradually change from local failure to structural failure. Specifically, in the scenario of W=400 g, R=0.45 m, and T=120 mm ($T/W^{1/3}$=0.16, $R/W^{1/3}$=0.61), the local failure of the RC slab was slight, i.e., no spall, while the corresponding structural failure was moderate, i.e., SR=2.12 °. Since local failure was the focus of this study, we suggested that the application range of Eq. (17) should be limited to $R/W^{1/3}$<0.6.

For the air-backed RC slab, forty simulation cases were designed based on the 160 mm, 200 mm, and 240 mm thickness RC slabs. Fig. 32 gives the simulation cases and simulated failure modes of the air-backed RC slab under a UWCI explosion. The failure extent of the air-backed RC slab becomes severe with increasing $T/W^{1/3}$ and decreasing $R/W^{1/3}$. Eq. (17) presents the spall and breach limits of the air-backed RC slab under a UWCI explosion, which agree with the simulation results (Fig. 32(b)). Note that the application range should be limited to $R/W^{1/3}$<2.4 since the structural failure is more significant than the local failure with the further increased

$R/W^{1/3}$. Comparison between the predictions of Eqs. (16) and (17) shows that the air-backed RC slab is much more susceptible to the UWCI explosion than the water-backed RC slab. When $R/W^{1/3}$=0.3, the air-backed RC slab must be 1.7 and 2.0 times thicker than the water-backed slab to prevent spall and breach failures, respectively, under a UWCI explosion. Additionally, compared to the in-air close-in explosion when $R/W^{1/3}$=0.3, the thickness of the air-backed RC slab needs to increase by 4.4 and 6.3 times to avoid spall and breach failures under a UWCI explosion. Hence, using the RC structure to resist a UWCI explosion may not be economical. It is necessary to design a novel structural form to alleviate the destructive effect of the UWCI explosion, such as ultra-high performance concrete (Zhou et al., 2023a; 2022b), foam concrete (Shi et al., 2023), CFRP (Yang et al., 2023a), or slurry-infiltrated fiber concrete (Li et al., 2023). This needs further study.

Spall limit(water-backed): $\frac{T}{W^{1/3}}=0.07\left(\frac{R}{W^{1/3}}\right)^{-1.4}$ (16a)

Breach limit (water-backed): $\frac{T}{W^{1/3}}=0.086\left(\frac{R}{W^{1/3}}\right)^{-0.7}$ (16b)

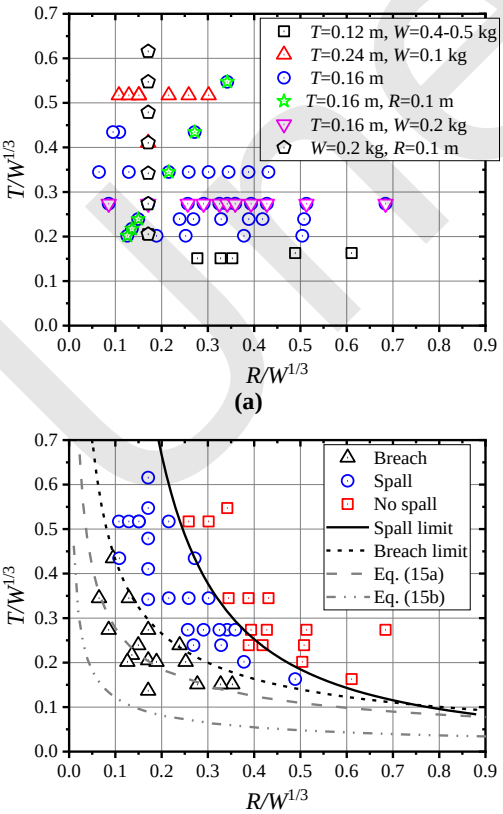

(b)

Fig. 31 Water-backed RC slabs under UWCI explosions: (a) simulation scenarios (b) failure modes

Spall limit (air-backed): $\frac{T}{W^{1/3}}=0.3\left(\frac{R}{W^{1/3}}\right)^{-0.64}$ (17a)

Breach limit (air-backed): $\frac{T}{W^{1/3}}=0.245\left(\frac{R}{W^{1/3}}\right)^{-0.42}$ (17b)

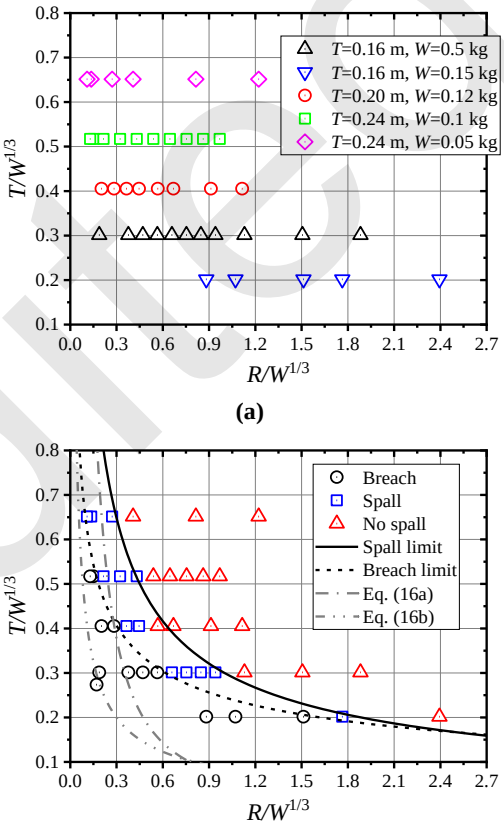

(b)

Fig. 32 Air-backed RC slabs under UWCI explosions: (a) simulation scenarios (b) failure modes

5 Conclusions

Based on an improved dynamic constitutive model calibrated for saturated concrete and a validated high-fidelity finite element analysis approach, this study numerically examined the local failure of an RC slab subjected to an underwater close-in explosion. The effects of some critical parameters were assessed, and formulae to predict the spall and breach limits were proposed for the water-backed and air-backed RC slabs according to extensive simula-

tions. The main conclusions are summarized as follows:

1. An improved dynamic constitutive model of concrete recently proposed by the authors was used for saturated concrete. The effect of free water content on the static and dynamic mechanical properties, including uniaxial tensile strength, uniaxial compressive strength, biaxial compressive strength, elastic modulus, strain rate effect, failure strength surface, and equation of state, of wet concrete were comprehensively calibrated according to experimental observations. A single-element test confirmed that the calibrated parameter could accurately reproduce the mechanical property of saturated concrete.

2. An arbitrary Lagrangian-Eulerian algorithm and the calibrated constitutive model for saturated concrete were used to further establish the high-fidelity finite element analysis approach for an RC slab subjected to underwater close-in explosion. The rationality of the finite element analysis approach was validated by simulating RC orifice targets subjected to underwater close-in explosion and a saturated concrete panel against underwater contact explosion. The simulation results indicated that the pressure time histories of the shock wave in water and the local failure dimension of the orifice targets and saturated concrete slab were precisely reproduced.

3. Based on the validated finite element analysis approach, we designed a baseline scenario of a 160-mm-thickness RC slab subjected to an underwater explosion of 200 g at a standoff distance of 100 mm and assessed the corresponding local and structural failure. The parametric study showed that the local failure of the RC slab subjected to underwater close-in explosion increased with increasing charge weight, reduced standoff distance, and reduced structural thickness. Compared to the water-backed RC slab, the air-backed RC slab exhibited much more obvious local and structural failure due to the difference in wave impedance.

4. We conducted over ninety simulation cases with different combinations of the structural thickness, charge weight, and standoff distance for the water- and air-backed RC slabs. The empirical formulae to determine the spall and breach limits were summarized accordingly. At a scaled distance of 3, compared to the empirical predictions for the in-air close-in explosion, the structural thickness of the RC slab needed to be increased by 3.1 for the water-back and 6.3 times for the air-back conditions subjected to the underwater close-in explosion to avoid a breach failure. These results suggest an opportunity to alleviate the destructive effects by using novel structures and materials in future studies.

Acknowledgements

This study was supported by the National Natural Science Foundation of China (52208500).

Author contributions

Fei ZHOU designed the research, wrote the first draft of the manuscript. Hedong LI helped to organize the manuscript. Hao WU revised and edited the final version.

Conflict of interest

Fei ZHOU, Hedong LI, and Hao WU declare that they have no conflict of interest.

References

Attard MM, Setunge S, 1996. Strain-stress relationship of confined and unconfined concrete. *ACI Materials Journal*, 93:432-442. https://doi.org/10.14359/9847

Chen ZJ, Zong ZH, Gan L, et al., 2023. Numerical investigation on dynamic response of air-backed RC slabs subjected to close-in underwater explosion. *Ocean Engineering*, 273:113962. https://doi.org/10.1016/j.oceaneng.2023.113962

Cole RH, 1948. Underwater Explosions. Princeton University Press, New Jersey.

Comite Euro-International Du Beton, 1993, CEB-FIP model code 1990: design code. https://doi.org/10.1680/ceb-fipmc1990.35430

Costanzo FA, 2011. Underwater Explosion Phenomena and Shock Physics. In: Proulx, T. (eds) Structural Dynamics, Volume 3. Conference Proceedings of the Society for Experimental Mechanics Series. Springer, New York, NY. https://doi.org/10.1007/978-1-4419-9834-7_82

Cui J, Hao H, Shi YC, et al., 2017. Experimental study of concrete damage under high hydrostatic pressure. *Cement and Concrete Research*, 100:140-152. https://doi.org/10.1016/j.cemconres.2017.06.005

Forquin P, Sallier L, Pontiroli C, 2015. A numerical study on the influence of free water content on the ballistic performances of plain concrete targets. *Mechanics of Materials*, 89:176-189. https://doi.org/10.1016/j.mechmat.2015.02.016

Gong H, Luo Y, Meng F, Du H, 2023. Failure behavior and strength deterioration model of high-performance concrete under coupled elevated temperature, biaxial constraint and impact loading. *Journal of Building Engineering*, 75: 107002. https://doi.org/10.1016/j.jobe.2023.107002

Hallquist J, 2006. LS-DYNA theory manual. Livermore Software Technology Corporation, 7374 Las Positas Road Livermore, California.

Hordijk DA, 1991. Local approach to fatigue of concrete. Ph.D. Thesis, Delft University of Technology, The Netherlands.

Hu J, Chen ZY, Zhang XD, et al., 2017. Underwater explosion in centrifuge part I: validation and calibration of scaling laws. *Science China Technological Sciences*, 60(11):1638-1657. https://doi.org/10.1007/s11431-017-9083-0

Huang X, Hu J, Zhang X, et al., 2020a. Bending failure of a concrete gravity dam subjected to underwater explosion. *Journal of Zhejiang University-SCIENCE A*, 21:976-991. https://doi.org/10.1631/jzus.A2000194

Huang X, Kong X, Hu J, et al., 2020b. The influence of free water content on ballistic performances of concrete targets. *International Journal of Impact Engineering*, 139:103530. https://doi.org/10.1016/j.ijimpeng.2020.103530

Klepaczko JR, Brara A, 2001. An experimental method for dynamic tensile testing of concrete by spalling. *International Journal of Impact Engineering*, 25(4):387-409. https://doi.org/10.1016/S0734-743X(00)00050-6

Kong XZ, Fang Q, Chen L, et al., 2018. A new material model for concrete subjected to intense dynamic loadings. *International Journal of Impact Engineering*, 120:60-78. https://doi.org/10.1016/j.ijimpeng.2018.05.006

Kumar V, Kartik KV, Iqbal MA, 2020. Experimental and numerical investigation of reinforced concrete slabs under blast loading. *Engineering Structures*, 206:110125. https://doi.org/10.1016/j.engstruct.2019.110125

Kupfer HB, Gerstle KB, 1973. Behavior of concrete under biaxial stresses. *Journal of the Engineering Mechanics Division*, 99(4):853-866. https://doi.org/10.1061/JMCEA3.0001789

Li H, Li Y, Pan Y, et al., 2023. Compressive properties of a novel slurry-infiltrated fiber concrete reinforced with arc-shaped steel fibers. *Journal of Zhejiang University-SCIENCE A*, 24:543-556. https://doi.org/10.1631/jzus.A2200405

Magnus D, Khan MA, Proud WG, 2018. Epidemiology of civilian blast injuries inflicted by terrorist bombings from 1970-2016. *Defence Technology*, 14(5):469-476. https://doi.org/10.1016/j.dt.2018.07.014

Malecot Y, Zingg L, Briffaut M, et al., 2019. Influence of free water on concrete triaxial behavior: The effect of porosity. *Cement and Concrete Research*, 120:207-216. https://doi.org/10.1016/j.cemconres.2019.03.010

Malvar LJ, Crawford JE, Wesevich JW, et al., 1997. A plasticity concrete material model for DYNA3D. *International Journal of Impact Engineering*, 19(9-10):847-873. https://doi.org/10.1016/S0734-743X(97)00023-7

McVay MK, 1988. Spall damage of concrete structures. Technical report SL88-22, U.S. Army Corps of Engineers Waterways Experimental Station.

Nord Stream Press Releases, 2022. Incident on the Nord Stream Pipeline [EB/OL]. https://www.nord-stream.com/press-info/press-releases/

Rajendran R, Lee JM, 2009. Blast loaded plates. *Marine Structures*, 22(2):99-127. https://doi.org/10.1016/j.marstruc.2008.04.001

Rankine WJM, 1876. A manual of applied mechanics. C Griffin and Co (London).

Ross CA, Jerome DM, Tedesco JW, et al., 1996. Moisture and strain rate effects on concrete strength. *Materials*, 93(3):293-300. https://doi.org/10.1016/0040-6090(95)08175-5

Sanders J, Urgessa G, Löhner R, 2021. Literature review on the response of concrete structures subjected to underwater explosions. CivilEng, 2(4), 895-908. https://doi.org/10.3390/civileng2040048

Sargin M, 1971. Stress-strain relationship for concrete and analysis of structural concrete sections. M.Z. Cohn (Ed.), Study N.4, Solid Mechanics Division, University of Waterloo, Waterloo (Ontario).

Shi S, Kong X, Fang Q, 2023. A plastic-damage material model for foam concrete under blast loads. *International Journal of Impact Engineering*, 177:104596. https://doi.org/10.1016/j.ijimpeng.2023.104596

Shi Y, Chen L, Wang Z, et al., 2015. Field tests on spalling damage of reinforced concrete slabs under close-in explosions. *International Journal of Protective Structures*, 6(2):389-401. https://doi.org/10.1260/2041-4196.6.2.389

Shi Y, Wang J, Cui J, 2020. Experimental studies on fragments of reinforced concrete slabs under close-in explosions. *International Journal of Impact Engineering*, 144:103630. https://doi.org/10.1016/j.ijimpeng.2020.103630

Simo JC, Hughes TJR, 1998. Computational inelasticity. New York: Springer.

Song G, Chen Z-Y, Long Y, 2017. Experimental and numerical investigation of the centrifugal model for underwater explosion shock wave and bubble pulsation. *Ocean Engineering*, 142:523-531. https://doi.org/10.1016/j.oceaneng.2017.04.035

Southpointe, 2020. ANSYS explicit dynamics analysis guide. ANSYS, Inc, Canonsberg, PA.

Tu ZG, Lu Y, 2009. Evaluation of typical concrete material models used in hydrocodes for high dynamic response simulations. *International Journal of Impact Engineering*, 36:132-146. https://doi.org/10.1016/j.ijimpeng.2007.12.010

UFC (Unified Facilities Criteria), 2008. 3-340-02 Structures to resist the effects of accidental explosions.

Wang W, Zhang D, Lu F, et al., 2012. Experimental study on scaling the explosion resistance of a one-way square reinforced concrete slab under a close-in blast loading. *International Journal of Impact Engineering*, 49:158-164. https://doi.org/10.1016/j.ijimpeng.2012.03.010

Wang H, Wang LC, Song YP, et al., 2016. Influence of free water on dynamic behavior of dam concrete under biaxial compression. *Construction and Building Materials*, 112:222-231.

https://doi.org/10.1016/j.conbuildmat.2016.02.090

Wen YB, Chi H, Lai ZC, et al., 2023. Experimental and numerical investigation on saturated concrete subjected to underwater contact explosion. *Construction and Building Materials*, 384:131465. https://doi.org/10.1016/j.conbuildmat.2023.131465

Wu S, Chen X, Zhou J, 2012. Influence of strain rate and water content on mechanical behavior of dam concrete. *Construction and Building Materials*, 36:448-457. https://doi.org/10.1016/j.conbuildmat.2012.06.046

Xu H, Wen HM, 2013. Semi-empirical equations for the dynamic strength enhancement of concrete-like materials. *International Journal of Impact Engineering*, 60:76-81. https://doi.org/10.1016/j.ijimpeng.2013.04.005

Xu H, Wen HM, 2016. A computational constitutive model for concrete subjected to dynamic loadings. *International Journal of Impact Engineering*, 2016, 91:116-125. https://doi.org/10.1016/j.ijimpeng.2016.01.003

Xu JP, Wu H, Ma LL, et al., 2022. Residual axial capacity of seismically designed RC bridge pier after near-range explosion of vehicle bombs. *Engineering Structures*, 265:114487. https://doi.org/10.1016/j.engstruct.2022.114487

Xu SL, Wu P, Zhou F, et al., 2020. A dynamic constitutive model of ultra high toughness cementitious composites. *Journal of Zhejiang University-SCIENCE A*, 21:939-960. https://doi.org/10.1631/jzus.A1900599

Yang GD, Wang GH, Lu WB, et al., 2019. Experimental and numerical study of damage characteristics of RC slabs subjected to air and underwater contact explosions. *Marine Structures*, 66:242-257. https://doi.org/10.1016/j.marstruc.2019.04.009

Yang GD, Fan Y, Wang GH, et al., 2022. Blast resistance of air-backed RC slab against underwater contact explosion. *Defence Technology*, In Press. https://doi.org/10.1016/j.dt.2022.11.004

Yang GD, Fan Y, Wang GH, et al., 2023a. Mitigation effects of air-backed RC slabs retrofitted with CFRP subjected to underwater contact explosions. *Ocean Engineering*, 267:113261. https://doi.org/10.1016/j.oceaneng.2022.113261

Yang GD, Fan Y, Wang GH, et al., 2023b. Experimental and numerical investigation on dynamic behavior of RC orifice targets subjected to underwater explosions. *Engineering Structures*, 279:115541. https://doi.org/10.1016/j.engstruct.2022.115541

Zhao FQ, Wen HM, 2018. Effect of free water content on the penetration of concrete. *International Journal of Impact Engineering*, 121:180-190. https://doi.org/10.1016/j.ijimpeng.2018.06.007

Zhao X, Wang G, Lu W, et al., 2018. Damage features of RC slabs subjected to air and underwater contact explosions. *Ocean Engineering*, 147:531-545. https://doi.org/10.1016/j.oceaneng.2017.11.007

Zhao X, Wang G, Lu W, et al., 2021. Experimental investigation of RC slabs under air and underwater contact explosions. *European Journal of Environmental and Civil Engineering*, 25(1):190-204. https://doi.org/10.1080/19648189.2018.1528892

Zhou F, Su Q, Cheng YH, et al., 2022. Novel constitutive model of UHPC under impact and blast loadings considering compaction of shear dilation. *International Journal of Impact Engineering*, 173:104468. https://doi.org/10.1016/j.ijimpeng.2022.104468

Zhou F, Su Q, Cheng YH, et al., 2023a. A novel dynamic constitutive model for UHPC under projectile impact. *Engineering Structures*, 280:115711. https://doi.org/10.1016/j.engstruct.2023.115711

Zhou F, Cheng YH, Peng Q, et al., 2023b. Influence of steel reinforcement on the performance of an RC structure subjected to a high-velocity large-caliber projectile. *Structures*, 54:716-731. https://doi.org/10.1016/j.istruc.2023.05.096

Zhou F, Wu H, Cheng YH, 2023c. Perforation studies of concrete panel under high velocity projectile impact based on an improved dynamic constitutive model. *Defence Technology*, 27: 64-82. https://doi.org/10.1016/j.dt.2022.09.004

Zhou F, Wu H, 2023. A novel three-dimensional modified Griffith failure criterion for concrete. *Engineering Fracture Mechanics*, 284:109287. https://doi.org/10.1016/j.engfracmech.2023.109287.

中文概要

题　目： 水中近场爆炸下钢筋混凝土板局部破坏模式数值模拟研究

作　者： 周飞[1]，李贺东[2]，吴昊[1]

机　构： [1]同济大学，结构防灾减灾工程系，中国上海，200092；[2]浙江理工大学，建筑工程学院，中国杭州，310018；

目　的： 钢筋混凝土板是水下设施的主要承重构件，在水中近场爆炸下可能遭受严重的局部破坏，如开坑、震塌及开裂。本文旨在通过高精度数值仿真方法探讨水中近场爆炸下爆距、炸药质量、结构厚度和结构背面空气/水介质对混凝土板损伤破坏的影响规律，并总结水中近场爆炸下混凝土板破坏模式评估公式。

创新点： 1. 采用作者前期建立的新型混凝土动态本构模型，系统标定了含水混凝土本构模型参数；2. 采用任意拉格朗日-欧算法，建立了钢筋混凝土板在水中近场爆炸下的高精度模拟方法；3. 建立了水中近场爆炸下钢筋混凝土板损伤破坏分析模型，开展了参数分析并归纳出损伤破坏评估方法。

方　法： 1. 基于现有试验数据，对自由水含量对混凝土的抗拉/抗压强度、弹性模量、应变率效应、强度面、

状态方程的影响进行了综合标定；2. 通过模拟现有混凝土隧洞靶的水中近场爆炸试验和混凝土板的水下接触爆炸试验，对所建立的有限元分析方法再现水中爆炸荷载以及混凝土的开坑、开裂等损伤破坏的能力进行了验证；3. 通过参数分析，明确了爆距、炸药质量、结构厚度和结构背面空气/水介质对混凝土板损伤破坏的影响规律；4. 基于大量仿真分析，归纳出水中近场爆炸下混凝土板破坏模式评估公式。

结　论： 1. 系统标定的本构模型参数可准确描述饱和混凝土的动态力学性能；2. 建立的高精度数值模拟方法可准确描述近场爆炸作用下混凝土板的开坑、开裂及震塌破坏；3. 水中近场爆炸下混凝土板的局部破坏随着炸药质量的增加、爆距的减小和结构厚度的减小而增大；4. 与背面水介质相比，背面空气介质的混凝土板损伤破坏显著增加；5. 归纳的水中近场爆炸作用下混凝土板损伤评估方法，可用于相关水下设施的抗爆设计。

关键词： 钢筋混凝土板；水中近场爆炸；饱和混凝土；破坏模式；本构模型；数值仿真